Contract N00014-85-F-0066

AD-A193 619

## Development of Metastable Processing Paths
### for
### High Temperature Alloys

Semi–Annual Technical Report
submitted to
Defense Advanced Research Projects Agency (DoD)
for the period
October 1, 1987 through March 31, 1987

Contractor: Metallurgy Division
National Bureau of Standards
Gaithersburg, MD

Principal Investigator: William J. Boettinger
301–975–6160

Senior Project Scientists: Leonid A. Bendersky
Benjamin A. Burton
John W. Cahn
Ursula R. Kattner
Robert J. Schaefer

DTIC
ELECTE
MAY 2 6 1988
S
D

Effective Date of Contract: February 9, 1987

Contract Expiration Date: December 31, 1989

Amount of Contract: $600,000

ARPA Order Number: 6065

Program Code Number: 7D10

88 5 13 035

Table of Contents

Summary

The possibility of developing new processing strategies for high temperature intermetallic compounds is being investigated. In particular rapid solidification followed by controlled heat treatment may provide new and unusual microstructures of multiphase materials. This report describes research performed at NBS to develop predictive models for solubility extension and metastable phase formation of intermetallic compounds and research to improve the phase diagram modeling of systems involving ordered phases.

Theory has been developed to treat the formation of disordered variants of intermetallic compounds during rapid solidification. Using a modification of the Aziz solute trapping theory, solidification velocities required to form, for example, a BCC phase from the melt when a B2 phase is the stable phase have been developed.

Experimental research has continued on two intermetallic systems, $Al_3Nb$ and NiAl–NiTi, using melt spinning and examination by transmission electron microscopy. In the case of $Al_3Nb$, which is considered a line compound, examination by TEM suggested that solubility extension was not obtained by melt spinning. Detailed x–ray diffraction analysis has confirmed this result and established the equilibrium width of the compound at 500° C. In the NiAl–NiTi system, the equilibrium intermediate Heusler phase, $Ni_2AlTi$, was suppressed by rapid solidification and extension of the composition range of the NiAl and NiTi phases was observed. To quantify the solidification rates required for this process, samples have been prepared for pulsed laser melting where the solidification rate can be varied between 1–10 m/s.

Experimental work on ternary alloys surrounding the composition $Ti_2NbAl$ have been initiated to determine the phases present in arc melted and heat treated samples. TEM investigations are required to sort out the complex ordering reactions in this important alloy system. Preliminary efforts have been focussed on reliable melting and

3

heat treatment procedures.

An evaluation of existing data and a thermodynamic calculation of the Ti–Al–Nb phase diagram have been performed using the THERMOCALC code.

I. Introduction

The development of high temperature materials is closely related to the formulation of processing strategies for chemically ordered phases. Most intermetallic compounds including aluminides, carbides, and silicides as well as high temperature ceramic phases are ordered. However, optimum mechanical properties are likely to come from intimate dispersions of several phases, some of which are ordered. These dispersions can be produced by a phase transformation sequence involving both ordering and phase separation beginning with a solid phase of a carefully selected unstable composition made by rapid solidification.

Recently, significant advances have occurred in the utilization and understanding of rapid solidification processing of alloys. Factors which promote refined segregation, solubility extension and metastable phase formation have been identified. However, much of this research has been focused towards disordered crystalline phases: i.e., terminal solid solutions, not ordered intermetallic compounds.

At the same time, significant advances have been realized in the thermodynamics and kinetics of order–disorder transitions. The distinction between first and higher order transitions has been clarified, the kinetics of ordering reactions and the structure and mobility of APB's have been determined and reactions that involve fine scale ordering and compositional separation have been studied.

This research attempts to combine the advances in these areas to develop new processing strategies for high temperature ordered multiphase materials.

In section II of this report we describe theoretical and experimental research focused

on determining the possibility of extending the solubility range of ordered phases by rapid solidification. Subsequent heat treatment of these metastable alloys can form stable high temperature multiphase mixtures. This research also includes an examination of the state of nonequilibrium order of rapidly quenched intermetallic compounds.

Section III of this report summarizes initial efforts at phase identification in composition surrounding $Ti_2NbAl$.

Section IV of this report describes phase diagram activities involving ordered phases. A calculation of the ternary diagram Ti–Nb–Al has been performed. Cluster Variation Methods (CVM) are also being developed for application to phase boundaries between ordered and related disordered BCC phases.

## II. Solubility Extension and Disordering of Intermetallic Compounds by Rapid Solidification

### (a) Theory of Disorder Trapping by Rapid Solidification

A model is developed to predict the long range order parameter and composition of a chemically ordered phase as a function of interface velocity. The model is an extension of the solute trapping model of Aziz and relies on an analysis of the interdiffusion across the liquid solid interface between a liquid phase and a solidcomposed of two sublattices. The model predicts the transition from solidification of a solid phase with equilibrium long range order parameter and with equilibrium partitioning of composition at low interface velocity to solidification of a disordered crystalline solid with the same composition as the liquid at high solidification velocity. Results for a Bragg Williams solid phase suggest that solute trapping and disorder trapping can occur at different growth rates.

The kinetics of the interface between phases during first order phase transitions, including solidification, have received considerable attention. Recent interest in the

processing of alloys and other materials using transitions far from equilibrium has renewed interest in these kinetics. Theories of nonequilibrium incorporation of solute into rapidly growing crystals are currently the focus of experimental test. An interesting additional possibility occurs for crystals with long range chemical order or intermetallic compounds. Rapid growth can also cause the formation of crystals with nonequilibrium long range order. Because ordering in the solid state during post–solidification cooling can mask events at the liquid solid interface, clearcut experimental results are difficult to design. However the observation of solidified phases with high densities of antiphase domains when the phase is normally ordered to the melting point is a clear indication that disorder has been trapped by the solidification process.

Kinetic theories generally fall into three categories: chemical reaction rate, diffuse interface, and statistical mechanics theories. Several diffuse interface theories have been able to predict in a formal way that disorder can be induced into a growing phase by rapid interface motion. None treats the simultaneous trapping of solute and disorder. The present paper describes a chemical reaction rate theory for the kinetics of crystallization of an ordered phase. The temperature, composition and order parameter of the solid will be described as a function of interface velocity and liquid composition. First, the conditions for equilibrium between a liquid and a solid phase consisting of two equivalent sublattices are reviewed; second the kinetic model is described; and finally predictions for the growth of a Bragg–Williams solid phase are presented.

Thermodynamics of the Phases at Equilibrium – We assume for simplicity that the solid phase consists of two equivalent sublattices $\alpha$ and $\beta$ and that a total free energy function for the solid, $G^T$ is a function of $n_i^j$, the number of moles of component i (i = A,B) on sublattice j (j = $\alpha,\beta$). The constraint of equal number of lattice sites of the two sublattices requires that $n_A^\alpha + n_B^\alpha = n_A^\beta + n_B^\beta$. One can formally define the chemical

potential of component i on the j sublattice as

$$\mu_i^j = \frac{\partial G^T}{\partial n_i^j}.$$  [1]

The conditions for equilibrium in the solid phase are given by

$$\mu_B^\alpha - \mu_A^\alpha = \mu_B^\beta - \mu_A^\beta.$$  [2]

If we assume that the constraint on the number of moles on each sublattice also holds in the solid at an interface with a liquid phase then one obtains at equilibrium

$$\frac{1}{2}(\mu_A^\alpha + \mu_A^\beta) = \mu_A^L$$
$$\frac{1}{2}(\mu_B^\alpha + \mu_B^\beta) = \mu_B^L$$  [3]

where $\mu_A^L$ and $\mu_B^L$ are the chemical potentials of the liquid phase. As a consequence of these three above conditions, the conditions

$$\mu_B^\alpha - \mu_A^\alpha = \mu_B^L - \mu_A^L$$
$$\mu_B^\beta - \mu_A^\beta = \mu_B^L - \mu_A^L$$  [4]

also hold at equilibrium. These conditions must be satisfied at the zero growth velocity limit of any kinetic theory.

The free energy of the solid phase is usually written on a molar basis, $G_m^S$, in terms of the compositions of A and B atoms on the $\alpha$ and $\beta$ sublattices, $x_A^\alpha$, $x_B^\alpha$, $x_A^\beta$, $x_B^\beta$ given by

$$x_A^\alpha = x_A^S + \frac{1}{2}\eta$$
$$x_A^\beta = x_A^S - \frac{1}{2}\eta$$
$$x_B^\alpha = x_B^S - \frac{1}{2}\eta$$
$$x_B^\beta = x_B^\beta + \frac{1}{2}\eta.$$  [5]

The long range order parameter, $\eta$ is given by

$$\eta = x_A^\alpha - x_A^\beta = x_B^\beta - x_B^\alpha$$  [6]

and the solid compositions, $x_A^S$, $x_B^S$, are given by

$$x_A^S = \tfrac{1}{2}(x_A^\alpha + x_A^\beta)$$

$$x_B^S = \tfrac{1}{2}(x_B^\alpha + x_B^\beta) \qquad [7]$$

where clearly, $x_A^\alpha + x_B^\alpha = 1$, $x_A^\beta + x_B^\beta = 1$, $x_A^S + x_B^S = 1$. With these definitions of composition the molar free energy $G_m^S$ is given by

$$G_m^S = \tfrac{1}{2}(\mu_A^\alpha x_A^\alpha + \mu_B^\alpha x_B^\alpha + \mu_A^\beta x_A^\beta + \mu_B^\beta x_B^\beta) \qquad [8]$$

If $G_m^S$ is treated as a function of the variables $x_B^\alpha$ and $x_B^\beta$ then

$$\mu_B^\alpha - \mu_A^\alpha = 2 \frac{\partial G_m^S}{\partial x_B^\alpha} \qquad [9]$$

$$\mu_B^\beta - \mu_A^\beta = 2 \frac{\partial G_m^S}{\partial x_B^\beta} \qquad [10]$$

and

$$\tfrac{1}{2}(\mu_A^\alpha + \mu_A^\beta) = G_m^S - x_B^\alpha \frac{\partial G_m^S}{\partial x_B^\alpha} - x_B^\beta \frac{\partial G}{\partial x_B^\beta} \qquad [11]$$

$$\tfrac{1}{2}(\mu_B^\alpha + \mu_B^\beta) = G_m^S + (1 - x_B^\alpha) \frac{\partial G_m^S}{\partial x_B^\alpha} - (1 - x_B^\beta) \frac{\partial G_m^S}{\partial x_B^\beta}. \qquad [12]$$

If on the other hand independent variables, $x_B^S$ and $\eta$, are used

$$\mu_B^\alpha - \mu_A^\alpha = \frac{\partial G_m^S}{\partial x_B^S} - 2 \frac{\partial G_m^S}{\partial \eta} \qquad [9']$$

$$\mu_B^\beta - \mu_A^\beta = \frac{\partial G_m^S}{\partial x_B^S} + 2 \frac{\partial G_m^S}{\partial \eta} \qquad [10']$$

and

$$\tfrac{1}{2}(\mu_A^\alpha + \mu_A^\beta) = G_m^S - x_B^S \frac{\partial G_m^S}{\partial x_B^S} - \eta \frac{\partial G_m^S}{\partial \eta} \qquad [11']$$

$$\tfrac{1}{2}(\mu_B^\alpha + \mu_B^\beta) = G_m^S + (1 - x_B^S) \frac{\partial G_m^S}{\partial x_B^S} - \eta \frac{\partial G_m^S}{\partial \eta}. \qquad [12']$$

<u>A Kinetic Model for the Interface – The Solidification Velocity–Composition</u>
<u>Relation</u> – We treat here the case of steady state continuous growth of an atomically
rough planar liquid–solid interface. Following the work of Aziz for random crystalline
solids, the atomistic interdiffusion flux between adjacent liquid and solid monolayers must
have a specific value ralated to the growth rate and the compositions of the monolayers in
order to maintain the steady state. For the growth of an ordered phase, the interdiffusion
flux between the liquid and each sublattice must be considered.

To treat interdiffusion between the liquid and solid phase during crystallization we
use redistribution potentials $(\mu_B - \mu_A)'$ as defined by Aziz[1]; viz.,

$$(\mu_B - \mu_A)' = \mu_B - \mu_A - RT \ln x_B - RT \ln x_A. \qquad [13]$$

We require redistribution potentials for the liquid phase, $(\mu_B^L - \mu_A^L)'$, and the $\alpha$ and $\beta$
sublattices of the solid phase, $(\mu_B^\alpha - \mu_A^\alpha)'$ and $(\mu_B^\beta - \mu_A^\beta)'$ from a thermodynamic model of
the phases. We consider a pair of reactions from initial states (of B in an $\alpha$ or $\beta$ site in
the solid adjacent to A in the liquid) over a barrier to final states (where the two atoms
have exchanged positions) as shown in Figure 1. The forward reactions are designated,
$J_D^{+\alpha}$ and $J_D^{+\beta}$, and the reverse reactions, $J_D^{-\alpha}$ and $J_D^{-\beta}$, and will be expressed in exchanges
per unit time per unit area of $\alpha$ (or $\beta$) sublattice. Although other choices are possible, the
interdiffusion flux from the state with the higher redistribution potential will be assumed
to be governed by a barrier height, $Q_D$, and the opposite flux will be governed by the
increased barrier height, $Q_D + |(\mu_B^i - \mu_A^i)' - (\mu_B^L - \mu_A^L)'|$ for i = $\alpha$, $\beta$. Thus, the
interdiffusion fluxes are given by

---

[1]Redistribution potentials can also be written in terms of activity coefficients $\gamma_A$, $\gamma_B$ and
free energies of the pure components $G_A$, $G_B$ as $(\mu_B - \mu_A)' = G_B - G_A + RT \ln \gamma_B$
$- RT \ln \gamma_A$.

$$J_D^{+\alpha} = \frac{f\nu\lambda}{\Omega} x_B^{\alpha}(1 - x_B^L) \exp\left[\frac{-[Q_D + A_\alpha|(\mu_B^\alpha - \mu_A^\alpha)' - (\mu_B^L - \mu_A^L)'|]}{RT}\right]$$

$$J_D^{-\alpha} = \frac{f\nu\lambda}{\Omega} x_B^{L}(1 - x_B^\alpha) \exp\left[\frac{-[Q_D + (1 - A_\alpha)|(\mu_B^\alpha - \mu_A^\alpha)' - (\mu_B^L - \mu_A^L)'|]}{RT}\right]$$

$$J_D^{+\beta} = \frac{f\nu\lambda}{\Omega} x_B^{\beta}(1 - x_B^L) \exp\left[\frac{-[Q_D + A_\beta|(\mu_B^\beta - \mu_A^\beta)' - (\mu_B^L - \mu_A^L)'|]}{RT}\right] \quad [14]$$

$$J_D^{-\beta} = \frac{f\nu\lambda}{\Omega} x_B^{L}(1 - x_B^\beta) \exp\left[\frac{-[Q_D + (1 - A_\beta)|(\mu_B^\beta - \mu_A^\beta)' - (\mu_B^L - \mu_A^L)'|]}{RT}\right]$$

where the parameters $A_i$ are introduced to yield the assumed barrier heights if

$$A_i = \begin{cases} 0 \text{ if } (\mu_B^i - \mu_A^i)' - (\mu_B^L - \mu_A^L)' \geq 0 \\ \\ 1 \text{ if } (\mu_B^i - \mu_A^i)' - (\mu_B^L - \mu_A^L)' < 0 . \end{cases} \quad [15]$$

The parameter f is the fraction of sites at the interface where jumps can occur, $\nu$ is the attempt frequency, $\lambda$ is the jump distance, and $\Omega$ is the atomic volume (assumed the same for A and B). This assumption regarding the barrier heights is identical to that made by Aziz. It implies that the exchanges are governed by the properties of the interface and not the bulk solid or liquid phases. One also could have introduced separate $Q_D^\alpha$ and $Q_D^\beta$ for the exchanges from the two sublattices, the consequences of which will be deferred to the discussion section of this paper.

The net diffusive fluxes, $J_D^\alpha$, and $J_D^\beta$, are then

$$J_D^\alpha = J_D^{+\alpha} - J_D^{-\alpha}$$

$$= D_i/(\lambda\Omega)[x_B^\alpha(1 - x_B^L)K_\alpha^{A_\alpha} - x_B^L(1 - x_B^\alpha)K_\alpha^{(1 - A_\alpha)}] \quad [16]$$

and $J_D^\beta = J_D^{+\beta} - J_D^{-\beta}$

10

$$= D_i/(\lambda\Omega)[x_B^{\beta}(1 - x_B^L)K_{\beta}^{\Lambda_{\beta}} - x_B^L(1 - x_B^{\beta})K_{\beta}^{(1 - \Lambda_{\beta})}] \qquad [17]$$

where

$$K_{\alpha} = \exp\left[\frac{-|(\mu_B^{\alpha} - \mu_A^{\alpha})' - (\mu_B^L - \mu_A^L)'|}{RT}\right]$$

$$K_{\beta} = \exp\left[\frac{-|(\mu_B^{\beta} - \mu_A^{\beta})' - (\mu_B^L - \mu_A^L)'|}{RT}\right] \qquad [18]$$

and as

$$D_i = f\nu\lambda^2 \exp\left\{-\frac{Q_D}{RT}\right\}. \qquad [19]$$

which is called the interface diffusivity.

In order to maintain steady state conditions at the growing interface a mass balance must be satisfied. In order to extract a simple model we will assume that interdiffusion in the liquid is fast enough to prevent lateral composition variations in the first liquid monolayer and that interdiffusion in the solid is slow enough that lateral exchanges (ordering) in the first solid monolayer do not occur. In this case mass balance requires that

$$J_D^{\alpha} = \frac{V}{\Omega}(x_B^L - x_B^{\alpha})$$
$$J_D^{\beta} = \frac{V}{\Omega}(x_B^L - x_B^{\beta}). \qquad [20]$$

where V is the interface velocity. Equating expressions for the net diffusive fluxes we obtain

$$x_B^{\alpha}(1 - x_B^L)(K_{\alpha})^{A_{\alpha}} - x_B^L(1 - x_B^{\alpha})K_{\alpha}^{(1 - A_{\alpha})} = \frac{V}{V_D}(x_B^L - x_B^{\alpha})$$

$$x_B^{\beta}(1 - x_B^L)K_{\beta}^{A_{\beta}} - x_B^L(1 - x_B^{\beta})K_{\beta}^{(1 - A_{\beta})} = \frac{V}{V_D}(x_B^L - x_B^{\beta}). \qquad [21]$$

where $V_D = D_i/\lambda$.

One may choose to solve these equations for a given V and $x_B^L$ in order to find the compositions of the $\alpha$ and $\beta$ sublattices. This would yield the average solid composition

and the long range order parameter at the interface. For this purpose we require the redistribution potentials which depend on temperature and the various compositions through a specific thermodynamic model of the liquid and solid phases. We also require an additional equation to relate the solidification velocity to the driving force for solidification.

The Solidification Velocity–Temperature Relation – It is often assumed that the solidification velocity V is related to the free energy change for crystlalization of $\Delta G$ according to

$$V = V_C \left[ 1 - \exp\left(-\frac{\Delta G}{RT}\right) \right] \qquad [22]$$

where $V_C$ is a crystallization rate parameter. In the present case

$$\Delta G = [\tfrac{1}{2}(\mu_A^\alpha + \mu_A^\beta) - \mu_A^L]x_A^S + [\tfrac{1}{2}(\mu_B^\alpha + \mu_B^\beta) - \mu_B^L]x_B^S \qquad [23]$$

Thus, when given thermodynamic potentials for the phases and kinetic parameters $V_D$ and $V_C$, Eqns. [21] and [22] give the order parameter, liquid composition, and temperature at the interface for any solid composition and solidification velocity.

Results for a Bragg–Williams Solid Phase and a Regular Solution Liquid Phase – The molar free energy, $G_m^S$, for a phase with only near–neighbor interactions energy $\Omega^S$ and ideal entropy can be given by

$$G_m^S = \tfrac{1}{2}G_A^S(x_A^\alpha + x_A^\beta) + \tfrac{1}{2}G_B^S(x_B^\alpha + x_B^\beta)$$
$$+ \tfrac{1}{2}\Omega^S(x_A^\alpha x_B^\beta + x_A^\beta x_B^\alpha)$$
$$+ \tfrac{1}{2}RT \{x_A^\alpha \ell n\, x_A^\alpha + x_A^\beta \ell n\, x_A^\beta + x_B^\alpha \ell n\, x_B^\alpha + x_B^\beta \ell n\, x_B^\beta\}. \qquad [24]$$

For the free energy function given in Eqn. [24]

$$\mu_B^\alpha - \mu_A^\alpha = G_B^S - G_A^S + \Omega^S(x_A^\beta - x_B^\beta) + RT \{\ell n\, x_B^\alpha - \ell n\, x_A^\alpha\}$$
$$\mu_B^\beta - \mu_A^\beta = G_B^S - G_A^S + \Omega^S(x_A^\alpha - x_B^\alpha) + RT \{\ell n\, x_B^\beta - \ell n\, x_A^\beta\} \qquad [25]$$

or for the redistribution potentials,

$$(\mu_B^\alpha - \mu_A^\alpha)' = G_B^S - G_A^S + \Omega^S(x_A^\beta - x_B^\beta) = G_B^S - G_A^S + \Omega^S(x_A^S - x_B^S - \eta)$$

$$(\mu_B^\beta - \mu_A^\beta)' = G_B^S - G_A^S + \Omega^S(x_A^\alpha - x_B^\alpha) = G_B^S - G_A^S + \Omega^S(x_A^\circ - x_B^\circ + \eta) . \qquad [26]$$

For the liquid phase we will employ a regular solution model; viz.,

$$G_m^L = G_A^L x_A^L + G_B^L x_B^L + \Omega^L(x_A^L x_B^L) + RT\{x_A \ln x_A + x_B \ln x_B\} \qquad [27]$$

with

$$\mu_A^L = G_A^L + \Omega^L(x_B^L)^2 + RT \ln x_A^L$$
$$\mu_B^L = G_B^L + \Omega^L(x_A^L)^2 + RT \ln x_B^L \qquad [28]$$

and redistribution potential

$$(\mu_B^L - \mu_A^L)' = G_B^L - G_A^L + \Omega^L(x_A^L - x_B^L) \qquad [29]$$

Dependence of Order Parameter on Velocity at a Congruent Maximum – By assuming that $G_A^L - G_A^S = G_B^L - G_B^S$ one obtains a phase diagram which is symmetric about $x = \frac{1}{2}$. In addition if $\Omega^S < \Omega^L$ the phase diagram exhibits a (congruent) melting maximum at $x = \frac{1}{2}$. For this case where in addition $\Omega^L = 0$, a simple expression can be obtained from Eqns. [21]. For $x_B^L = \frac{1}{2}$, and $x_B^S = \frac{1}{2}$ both equations are identical and yield an expression for the order parameter valid for $\eta \geq 0$ given by

$$(1 - \eta) - (1 + \eta) K - 2\frac{V}{V_D} \eta = 0 \qquad [30]$$

where

$$K = \exp\{\frac{\Omega^S \eta}{RT}\} . \qquad [31]$$

Rearranging, one obtains

$$\frac{\Omega^S \eta}{RT} = \ln \left[ \frac{(1 - \eta) - 2\frac{V}{V_D}\eta}{1 + \eta} \right]. \qquad [32]$$

The equilibrium order parameter $\eta_e$ can be found by solving equation [2] using Eqns. 9', 10' and 26. For $x_B^S = \frac{1}{2}$, $\eta_e$ is given by

$$\frac{\Omega^S \eta_e}{RT} = \ell n \left[\frac{1 - \eta_e}{1 + \eta_e}\right] .$$ [33]

Hence $\frac{\Omega^S}{RT}$ can be eliminated from Eqn. [32] and

$$\left[\frac{1 - \eta_e}{1 + \eta_e}\right]^{1/\eta_e} = \left[\frac{(1 - \eta) - 2\frac{V}{V_D}\eta}{1 + \eta}\right]^{1/\eta}$$ [34]

or

$$\frac{V}{V_D} = \frac{1}{2}\left[\frac{1 - \eta}{\eta} - \frac{1 + \eta}{\eta}\left[\frac{1 - \eta_e}{1 + \eta_e}\right]^{\eta/\eta_e}\right]$$ [35]

where $\eta_e$ is the equilibrium order parameter at the temperature of the liquid–solid interface. It is interesting to note that as $\frac{V}{V_D} \to \frac{1}{2\eta_e} \ell n \left[\frac{1 + \eta_e}{1 - \eta_e}\right] - 1$, $\eta \to 0$. Hence the order parameter is reduced to zero at a velocity which depends on the equilibrium order parameter. The higher the equilibrium order parameter the higher the solidification velocity required to trap complete disorder. Figure 2 shows a plot of eqn. [34] for various values of $\eta_e$ and Figure 3 shows the velocity required to form a completely disordered solid as a function of the equilibrium order parameter at the solidus.

Dependence of Order Parameter and Liquid Composition on Velocity for Arbitrary Solid Composition – For compositions away from a congruent maximum, three simultaneous equations (Eqns. 20 and 21) must be solved. Figure 4 shows a symmetric equilibrium phase diagram for an ideal liquid and Bragg Williams solid phase with $T_c$ = 1500 K. The pure component melting temperatures are 1000 K and the pure component entropies of fusion are 2R.

Figure 5 shows the dependence of $\eta$ on V while Figure 6 shows the dependence of $x_B^L$ on V for a solid where $x_B^S = 0.415$ ($V_c$ has been set to $\infty$). Note the slight perturbation in the composition curve at the velocity where $\eta$ goes to zero.

14

(b) <u>Solubility Extension of a Line Compound (Al$_3$Nb)</u>

Previously, alloys of composition Al–22 at% Nb and Al–28 at% Nb were prepared

by arc melting. These alloys were ± 3 at% on either side of the compound Al$_3$Nb. Alloys

were melt spun on a Cu wheel in a He atmosphere. The produced ribbons were

electropolished and examined by transmission electron microscopy. Neither composition

was single phase indicating that solubility extension, if present, was less than 3 at%. The

Al–22 at% Nb ribbon microstructure consists of cells of the Al$_3$Nb phase surrounded by

FCC aluminum phase. The Al–28 at% Nb ribbons consist of cells of the Al$_3$Nb phase

surrounded by the $\sigma$(Al,Nb) phase. Both are the expected equilibrium structures given by

the phase diagram.

In order to establish more quantitatively whether any solubility extension was

achieved, x–ray powder diffraction was performed in the melt spun ribbons and on

equilibrated samples. The Al–28 at% Nb ribbons were heat treated at 500°C for 24 hrs

and water quenched. The Al–22 at% Nb ribbons were heat treated at 600°C for 24 hrs

and water quenched. Lattice parameters were obtained by Nelson–Riley extrapolation of

the 200, 220, 400 and 420 peaks to determine "a". A single 008 peak was used to

determine the "c" parameter. Other peaks could not be used because of overlaps with the

other phases present. The results are given in Table 1 along with the values from the

JCPDF files.

Table 1. <u>Summary of Diffraction Results on Al$_3$Nb Alloys</u>

|  | a(A) | c(A) | $a^2c(A^3)$ | Volume/atom ($A^3$) |
|---|---|---|---|---|
| Al–22 at% Nb ribbons | 3.8404 | 8.6112 | 127.00 | 15.88 |
| Al–22 at% Nb annealed | 3.8397 | 8.6104 | 126.95 | 15.87 |
| Al–28 at% Nb annealed | 3.8448 | 8.6088 | 127.26 | 15.91 |
| Al–28 at% Nb ribbons | 3.8458 | 8.6072 | 127.30 | 15.91 |
| Al$_3$Nb (JCPDF) | 3.8445 | 8.601 | 127.12 | 15.89 |

One can see that the $Al_3Nb$ phase in the melt spun ribbon is essentially identical to that in the annealed sample for each composition. The equilibrium width of the single phase $Al_3Nb$ region is certainly greater than any solubility extension. In order to gain an estimate of this range of equilibrium solubility, a plot given in Figure 1 was constructed. The volume/atom is plotted as a function of composition for the single phase regions in the Al–Nb system. One can see a good linear fit to the data from pure Nb to $Al_3Nb$. A minimum likely occurs in the plot between Al and $Al_3Nb$ reflecting the change in bonding of the Al atoms. Using the slope obtained from the Nb–rich phases the values in Table 1 can be convected to a composition range of 24.5 to 26.0 at% Nb for the $Al_3Nb$ phase at ~550°C. This estimate for the width of the $Al_3Nb$ single phase field should be a lower bound since any change in slope of the curve in Figure 1 to reach the atomic volume for pure Al would expand the estimate for the range of stoichiometry for $Al_3Nb$.

Although these initial attempts to extend the solubility of a line compound by rapid solidification were unsuccessful, future work is planned with alloys using higher cooling rates.

### (c) Solubility Extension in the NiAl–NiTi System

Alloys belonging to the quasi–binary system containing NiAl, $Ni_2AlTi$, and NiTi were chosen for a study of solubility extension of intermetallic compounds with significant equilibrium ranges of solubility (non–line compounds). This specific alloy system was also chosen because Heusler phase based on the ideal composition $Ni_2AlTi(NiAl \cdot NiTi)$ has a crystal structure, $L2_1$ (identical to $DO_3$), which is an ordered form of the B2 structure. Although the solid state B2 to $DO_3$ transformation satisfies the Landau rules for an allowable higher order transition, the system contains a pair of two phase fields, $NiAl + Ni_2AlTi$ and $Ni_2AlTi + NiTi$, indicating that the transition is first order at those temperatures. These two–phase fields permit the study of solubility extension by rapid

16

solidification and an exploration of nonequilibrium ordered states and reaction paths.

Previous rapid solidification experiments using melt spinning have increased the solubility range of the B2 phases, NiAl and NiTi. More Ti was forced into the NiAl phase and more Al into NiTi phase than can be obtained by conventional solidification or solution heat treatment. This suggests a kinetic preference for the formation of the B2 phases over the $L2_1$ phase ($Ni_2AlTi$).

In collaboration with Professor Mike Aziz of Harvard, laser surface melting and resolidification experiments are being conducted to determine the limits of non-equilibrium processing of the $Ni_2AlTi$ composition. The solidification velocity to form the B2 phase from the melt instead of the equilibrium $L2_1$ phase will be determined. It is also anticipated that still higher solidification rates may form the BCC phase. The melting experiments are being performed with simultaneous reflectance measurement, thus enabling a measurement of melt duration. This permits an accurate assessment of solidification velocity without assumptions about laser power absorption. Since solid–state ordering may mask the state of order produced at the liquid solid interface in the solidified samples, a determination of the ABP displacement vector by TEM will be used to infer the original solidification product structure. Assuming the structure has ordered to $L2_1$, the presence of [001] and [111] APB's will indicate that BCC formed from the melt whereas the presence of only [001] APB's will indicate that B2 formed from the melt.

Solid state transformations are quite rapid in this alloy system. The supersaturated B2 orders continuously into single phase $L2_1$ during the solid state cooling of the melt spinning process. Subsequent heat treatment develops two phase microstructures of $B2 + L2_1$. A preprint of a paper on the effect of coherency strains on the kinetics of this process is included in the Appendix.

## III. Experimental Studies of the Ti-Al-Nb System

Titanium Aluminide with ~10 at% Nb additions have demonstrated interesting high temperature creep and oxidation properties. Research by Strychor, Williams and Soffa and also Banerjee have indicated the presence of a B2 and an orthorhombic ordered phase located around the composition $Ti_2NbAl$. We have initiated a systematic study of alloys in this region to determine the phases present in arc cast, melt spun and heat treated samples with the goal of determining the stable and metastable equilibria. This effort is coordinated with the phase diagram activities at the University of Wisconsin by J. Perepezko and Y. A. Chang.

To date difficulties with ingot homogeneity have been solved and a high temperature (2000° C) furnace with high purity Argon atmosphere has become operational. The alloys under investigation are given in Table 2.

Table 2. Ti-Al-Nb Alloys Under Investigation

| Ingot # | at% Ti | at% Al | at% Nb |
|---------|--------|--------|--------|
| 033088  | 50     | 25     | 25     |
| 040188  | 50     | 12.5   | 37.5   |
| 040288  | 37.5   | 25     | 37.5   |
| 040388  | 62.5   | 25     | 12.5   |
| 040488  | 50     | 37.5   | 12.5   |

## IV. Phase Diagram Modeling

There has always been a significant gap between the efforts of phase diagram modelers and measured phase diagram data. First principle approaches do not presently have great usefulness for the development of unique processing strategies. However, significant advances have recently occurred for phase diagram modeling using another approach. Existing phase diagram and thermodynamic data, which often exist only in limited composition or temperature ranges, can be fitted using free energy functions based

on reasonable physical models of phases with adjustment of parameters which relate to these physical models. Although phase diagrams based on such modeling can never replace carefully measured diagrams, they do provide a thermodynamically consistent first approximation to the equilibrium diagram. They provide two types of information. Choices of composition and temperature can be determined for critical expeirments which minimize the number of alloys prepared. Qualitative features of metastable phase diagrams can be used to guess general processing strategies for specific alloy systems without a knowledge of the precise location of phase boundaries.

For ordered intermetallic phases three methods are available for modeling the free energy and hence phase diagrams. Landau expansions are useful to determine qualitative features of phase transformation near critical points. Sublattice or Bragg–Williams models are useful for describing phases where the difference in size, charge or electronegativity causes a deviation from random mixing of the atoms; i.e., the formation of long range order. It treats the phase like a regular solution with a number of sublattices. The third method involves the calculation of free energies by summing the energy of clusters of atoms (usually tetrahedral or octahedral) and is called the cluster variation method.

In the following two sections we describe (a) activities using existing phase diagram software (Thermocalc) which utilize the sublattice approach for a calculation of the Ti–Al–Nb ternary diagram, and (b) activities focussed towards a more physically realistic calculation of ordering in the BCC portion of the Ti–Al–Nb diagram and the Ni–Al–Ti diagram.

(a) Thermocalc description of the Ti–Al–Nb ternary phase diagram

A preliminary calculation of the Ti–Al–Nb ternary phase diagram was undertaken using the THERMOCALC DATABANK system described by B. Sundman, B. Jansson

and J. O. Andersson (CALPHAD 9, 2 (1985) pp. 153-190). The stability ranges were adjusted to match the preliminary experimental data obtained at the University of Wisconsin by J. H. Perepezko and Y. A. Chang under DARPA contract. Subsequent changes in the experimental data can be used to ammend the calculated diagram.

In the calculations of the binary systems the liquid and elemental phases were described as sub-regular solutions. The intermetallic compounds in the Nb-Al and Ti-Al were described with the Wagner-Schotky model, where intermetallic compounds are considered to consist of different sublattices allowing substitutional solutions on each of these sublattices. Since the Wagner-Schotky model is mathematically a special case of the sublattice model, the parameters of these intermetallic compounds can be easily transformed to the sublattice model description of the THERMOCALC DATABANK system.

For the extrapolation of ternary Ti-Nb-Al system all phases must be allowed to have ternary ranges of homogeneity, which means for the Wagner-Schotky phase that they have to be modeled as metastable phases for the two other binary systems.

As a first approximation the Gibbs energies of formation of the Nb-Al compounds in the Ti-Al system and the Ti-Al compounds in the Nb-Al system were assumed to be the same as in the system where these compounds are stable, for the Nb-Ti system the Gibbs energies of formation were assumed to be the same as for these compounds consisting only of Nb or Ti, respectively.

In order to prevent these metastable phases from becoming stable in the binary systems and to adjust the calculated phase diagram to experimental results at 1200°C, the Gibbs free energies of formation of these metastable phases were adjusted by assuming that the entropies of formation of the metastable phases have the same magnitude as the stable phases and the enthalpies of formation of the metastable phases are more positive

than those of the stable phases. The ternary ranges of homogeneity at 1200°C calculated with these parameters were acceptable except for the hcp and $Ll_0$ phase, where they were too small. This was adjusted by giving the Nb–Al interaction term of the hcp phase the most negative value possible, without the hcp–phase becoming stable in the Nb–Al system. For the $Ll_0$–phase ternary interaction terms were introduced between Al and Nb on the first sublattice and with Ti on the second one and between Al and Ti on the first sublattice and Nb on the second one.

The calculated binary diagrams used for the Ti–Nb–Al ternary calculation are shown in Figures 8, 9, and 10. The correct Ti–Al diagram is still subject to debate in some regions and can be modified at a later time.

The results obtained from the calculations with these parameters are shown in Figures 11, 12, and 13. Ternary phases were omitted at this initial stage. Figures 11 and 12 show isothermal sections at 800°C and 1200°C, while Figure 13 shows the liquidus projection. Figure 14 presents the reaction scheme derived from these diagrams. It is interesting to note that the $\gamma$ phase based on TiAl extends nearly to the composition $TiAl_2Nb$ (designated $\gamma'$ by Perepezko and Chang). It may be possible that these phases form a continuous series of composition of the same crystal structure.

Further work on phase diagram modeling in this system must await a more precise definition of the measured phase boundaries.

(b) <u>CVM Analysis of Ternary BCC Alloys</u>

A great majority of ordered structures which are considered useful as structural materials are based on ordering of BCC, FCC, and HCP lattices. In the research performed under this contract we intend to focus on the modeling of ordered phases in ternary alloys based on these three basic lattices. Real phase diagrams will be a superposition of these with one type being dominant over some range of composition

and/or temperature.

Initial efforts are being focussed on ternary alloys based on the BCC lattice. A computer program has been written to solve the cluster variation method (CVM) equations for the tetrahedron approximation (TA) in the $\epsilon$–G mode. With this program it is possible to model binary and ternary phase relations between A2, B2, B32, $DO_3$, and $L2_1$ phases (Table 3, Figure 15). An example of the basic cluster (largest cluster) for this approximation is shown in Figure 15 as the tetrahedron 1234. Pairwise interaction parameters for first– and second–nearest–neighbor atom pairs can be considered, and many–body interactions and long–range strain contributions may also be included.

Table 3. <u>Some Crystallographically Related Structures Built From BCC</u>

| Structure Type | Name | Example | Element in Position a | b | c | d |
|---|---|---|---|---|---|---|
| A2 | bcc | VRe | V or Re | V or Re | V or Re | V or Re |
| B2 | CsCl–binary | VOs | V | V | Os | Os |
| B2 | CsCl–ternary | $Ag_2TiAl$ | Ag | Ag | Al or Ti | Al or Ti |
| $L2_1$ | $Cu_2MnAl$ | $Cu_2MnAl$ | Cu | Cu | Mn | Al |
| $DO_3$ | $Fe_3Al$ | $Fe_3Al$ | Fe | Fe | Fe | Al |
| B32 | NaTl | LiAl | Li | Al | Al | Li |

In most cases it is sufficient to consider only first– and second–nn pairwise interactions, but there are exceptions. For example, in the pseudobinary NiAl–NiTi (and therefore the ternary Ni–Al–Ti) it is necessary to invoke either: (1) first–nn through third–nn pair interactions, or (2) long–range "strain" contributions, to successfully model the observed phase relations. Other possible applications include $Cu_3Al$–$Cu_2MnAl$ and Fe↑–Fe↓–Al = the system Fe–Al including magnetic interactions.

We are particularly interested in comparing our results with parallel THERMOCALC calculations that are based on the "sublattice model." The

THERMOCALC sublattice approach is more empirical (generally requires more variable parameters) and is therefore better suited to fitting large data sets. The CVM, $\epsilon$–G approach is better for evaluating the role of order–disorder phenomena, and for separating the contributions from short– and long–range interactions.

Program development and testing is now complete and numerical work on the NiAl–NiTi pseudobinary join is in progress. Also, the effects of long–range strain on binary phase relations are being evaluated since previous studies ignored this important contribution.

V. Fiscal Status

(1) Amount currently provided for contract program

$150,000 for period February 9, 1987 to September 30, 1987.

$200,000 for Period October 1, 1987 to September 30, 1988.

(b) Expenditure and commitment during October 1, 1987 to March 31, 1988

$100,000

(c) Estimated funds required to complete this work

| | |
|---|---|
| April to June 1988 | $50,000 |
| July to September 1988 | $50,000 |
| October to December 1988 | $50,000 |
| January to March 1989 | $50,000 |
| April to June 1989 | $50,000 |
| July to September 1989 | $50,000 |
| October to December 1989 | $50,000 |

Figure 11. Calculated isothermal section of the Ti–Al–Nb ternary phase diagram at 800°C omitting ternary phases.

Figure 12. Calculated isothermal section of the Ti–Al–Nb ternary phase diagram at 1200°C omitting ternary phases.

Figure 13. Calculated liquidus projection of the Ti–Al–Nb ternary phase diagram omitting ternary phases.

Figure 14. Reaction scheme for Ti–Al–Nb derived from the calculated liquidus projection and isothermal sections at 800°C and 1200°C.

Figure 15. The four atomic positions obtained by stacking eight small body–centered cubes. The sites a, b, c, d refer to the crystal structures in Table 3. The tetrahedron 1234 is an example of the basic cluster used for the CVM calculation. It includes first–neighbor interaction 1–3 and 2–4 as well as second–neighbor interaction 1–2 and 3–4.

APPENDIX

# THE ROLE OF ELASTIC ENERGY IN THE MORPHOLOGICAL DEVELOPMENT OF A Ni-Ti-Al ALLOY

L. A. Bendersky, P. W. Voorhees*, W. J. Boettinger, and W. C. Johnson#

Metallurgy Division, National Bureau of Standards, Gaithersburg, MD 20899
*Department of Materials Science and Engineering, Northwestern University, Evanston, IL 60201
#Department of Metallurgical Engineering and Materials Science, Carnegie-Mellon University, Pittsburgh, PA 15213-3890

## Introduction

Recently there has been renewed interest in the development of alloys based on intermetallic phases. One approach is to develop alloy systems consisting of two ordered phases (1). The processing of these systems necessary to obtain optimum microstructures requires an understanding of phase instabilities involving both order parameter and composition (2) as well as the coarsening behavior of these two-phase mixtures.

In this paper we describe the late-stage microstructural development of a rapidly solidified $Ni_{50}Al_{12.5}Ti_{37.5}$ alloy. Under ordinary processing conditions this alloy contains nearly equal volume fractions of a Ti-rich B2 phase based on NiTi and a Heusler ($L2_1$) phase based on $Ni_2TiAl$ (3). Following melt spinning the alloy is essentially metastable single phase Heusler, except for the possibility of the antiphase domain boundaries (APB's) being wet by a thin layer of the B2 phase (4). During heat treatment, the isotropic APB structure disappears and is replaced by an array of cuboidal precipitates of the Heusler phase in the B2 matrix. At very long aging times, the formerly distinct precipitates disappear and a isotropic interconnected structure appears. The appearance of the highly interconnected structure is linked to the nearly equal volume fractions of each phase and the loss of coherence at the Heusler-B2 interface. The change in microstructure associated with loss of coherence indicates that the transformation sequence is strongly influenced by stress. The lattice parameter difference between the B2 and Heusler phases (~1.6%) introduces large elastic strains when the system is coherent. We suggest that the effects of elastic energy can dominate the effects of interfacial energy and determine the precipitate shape, and that the elastic interaction energy between precipitates leads to the aligned structures. These elastically driven effects are reduced as the system loses coherency. We believe that the evolution of microstructure in this system can be understood on the basis of these strain effects.

## Experimental Procedure

The alloy was prepared by arc melting 99.99% pure components. Rapidly solidified samples were prepared by melt spinning in a He atmosphere on a Cu wheel. The evolution of the microstructure was studied by heat treating samples at 800°C for 10 min., 1 h, 10 h, and 100 h. TEM samples were prepared by twin jet electropolishing in 8% perchloric in acetic acid at room temperature.

The analyzed microstructures are either the Heusler ($L2_1$) phase with APB's or a mixture of Heusler and B2, with a common cubic lattice. Therefore imaging of microstructural detail is possible only in dark-field with a superlattice reflection. For imaging the Heusler phase and its APB's, we used the $111_H$ reflection at a foil orientation close to the <011> zone axis. For imaging the B2 phase, we used the $100_{B2}$ reflection (almost overlapping with $200_H$) at a foil orientation close to the [100] zone axis. Even though both reflections operate in dark-field imaging, the unexpected stronger scattering factor for $100_{B2}$ enabled us to image the B2 phase clearly.

In the following discussion, the results are analyzed in terms of a quasibinary NiTi-$Ni_2TiAl$ phase diagram (tie lines lie in the section). However, this is not completely correct since in addition to major transitions involving B2 and $L2_1$, a small fraction of grain boundary and volume precipitation of a third phase was also observed. Also, both B2 and Heusler phases have additional diffuse scattering localized at $(110_2)$, similar to that observed in CuMnAl alloys (5). These effects will be discussed elsewhere since they do not

affect the major conclusions of this work.

## Results and Discussion

The microstructure of the as-solidified melt-spun ribbon consists of 1-2 $\mu$m diameter columnar grains of an essentially single-phase Heusler structure. This is to be contrasted with arc melted buttons which are two phase (4). Figure 1 shows a typical grain where a relatively large density of antiphase domain boundaries is imaged. The boundaries are basically isotropic, although observation of foils at <001> zone axis orientation shows some alignment of APB's along {100} planes with signs of possible wetting by the B2 phase.

After annealing for 10 min. at 800°C, the Heusler phase decomposes into the two-phase structure shown in Figure 2. The alignment of the B2 phase along the elastically soft <100> directions is clear. The structure is most likely a result of chemical spinodal decomposition of the supersaturated Heusler phase into Al-rich regions and Ti-rich regions, with a characteristic wavelength of ~10 nm. The Ti-rich regions subsequently continuously disorder into the B2 structure in a manner similar to that described by Allen and Cahn [2]. Consistent with a spinodal decomposition process is the interconnectedness of the microstructure and the absence of readily identifiable "matrix" and "precipitate" phases. In addition, the interfaces between the precipitates and matrix appear diffuse, in contrast to those seen in long time anneals. The alignment of the structure is due to an orientational dependence of the elastic energy of the spinodal waves. This orientational dependence results in composition waves along the elastically soft <100> crystallographic directions (6).

The microstructure after a one hour anneal at 800°C is shown in Figure 3. In contrast to the microstructure shown in Figure 2, the precipitate and matrix phases are now readily identifiable as the Heusler and B2 phases, respectively, (using additional observation in a <011> zone axis orientation). We believe that the elastic field generated by the large precipitate-matrix misfit contributes to both the cuboidal morphology of the individual precipitates and the crystallographic alignment of the precipitates. A misfitting precipitate with a cuboidal morphology may possess a lower total energy than an ellipsoid when elastic effects are included even when the interfacial energy is isotropic (7). This view is reinforced when later we see the loss of the cuboidal morphology when the strain fields are relaxed. The elastic interaction between precipitates can also strongly affect the spatial distribution of the precipitates. Elastic energy calculations of cubes in isotropic media with different elastic constants than the matrix (7) and cubes in anisotropic media with the same elastic constants as the matrix (8) show that the elastic interaction energy between misfitting cuboids results in an effective force which is attractive at long distances and repulsive at short distances. As a result, the cubes tend to align face to face with a small distance of separation and do not coalesce. It is the repulsive force which is a result of the elastic interaction that prevents the cubes from touching. That the system is largely coherent is substantiated by Figure 4 where the widely spaced bulk dislocations are imaged in weak beam dark field with the fundamental $400_H$ reflection. There is no evidence of interface dislocations associated with a semi-coherent interface.

Aging for 10 hours at 800°C produces no radical change in the microstructure, other than an increase in the size of the precipitates. As shown in Figure 5, the cubes are still aligned along the crystallographically soft directions with small interparticle separations. However, there has been a change in the structure of the two-phase interface. Figure 6 shows a square net of interfacial dislocations. The dislocations are of edge type with Burgers vector $1/2a_o^H[100]$. The dislocation spacing, about 35 nm, is not enough to accommodate the misfit. Thus, despite the loss of coherency, the elastic energy is still sufficient to maintain the cuboidal morphology of the precipitates and the alignment of the individual precipitates.

Figure 7 shows the microstructure after 100 hours of aging. The aligned microstructure of cuboidal precipitates has disappeared entirely and an isotropic, interconnected microstructure has appeared. The cause of the microstructural change is related to the relaxation of the misfit strains by interfacial dislocations. This is illustrated in Figure 8 using dark-field weak-beam imaging to show the interphase structure. Clearly evident is the square network of interfacial dislocations of the $1/2a_o^H<100>$ edge type with a spacing of about 20 nm. This spacing of interfacial dislocations is sufficient to relax most of the misfit strain. Thus, the elastic interaction between the precipitates is now negligible and the raft-like arrangement of the precipitates is destabilized. As there is little barrier to

coalescence, since the ordered nature of the phases implies that the touching of two Heusler precipitates will result in the presence of a low energy APB only 50% of the time, an interconnected structure results which is characteristic of two phases with approximately equal volume fractions. The isotropy of the observed interconnected structure is likely a result of the nearly isotropic interfacial energy in this system.

We believe that these micrographs present conclusive evidence that the elastic strain energy is important in determining the morphological evolution in this system.

## Acknowledgements

## References

1. R. S. Polvani, W. S. Tzeng and P. R. Strutt, Met. Trans. 7A (1976) 33.
2. S. M. Allen and J. W. Cahn, Acta Met. 24 (1976) 425.
3. A. Taylor and P. W. Floyd, J. Inst. Metals 80 (1952-3) 25.
4. W. J. Boettinger, L. A. Bendersky, F. S. Biancaniello and J. W. Cahn, Mats. Sci. and Eng. (in press).
5. M. Bouchard and G. Thomas, Acta Met., 23, 1485 (1975).
6. J. W. Cahn, Trans. TMS-AIME, 242, 166 (1968).
7. William C. Johnson and P. W. Voorhees, J. Appl. Phys. 61, 1610 (1987).
8. A. G. Khachaturyan, S. V. Semenovskaya and J. W. Morris, Jr., Center for Advanced Materials Report, LBL, preprint #22472 (1986).
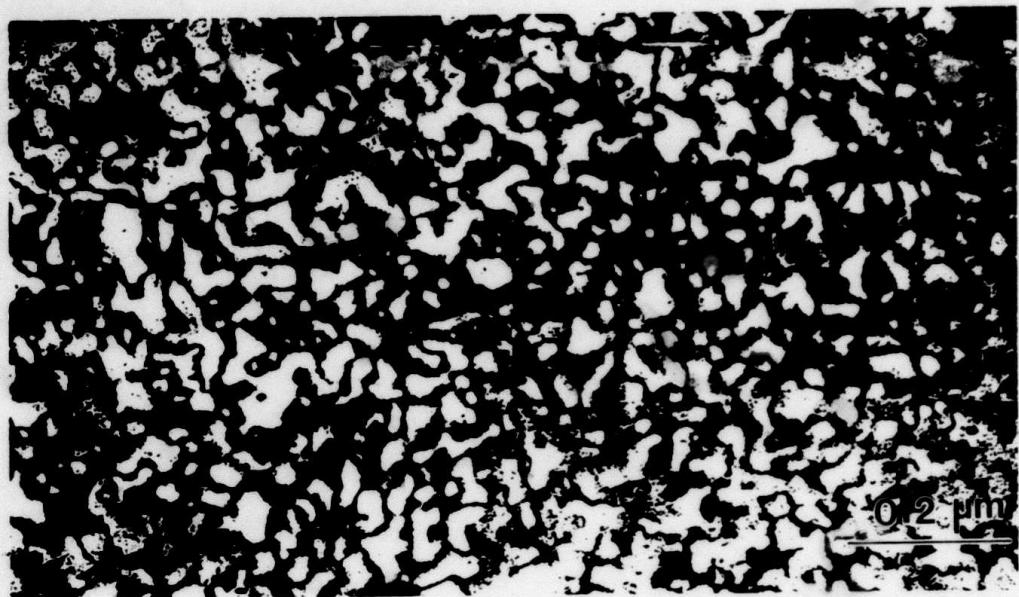
**Figure 1.** $111_H$ dark-field micrograph of the as-solidified melt spun alloy showing relatively isotropic orientation of $1/2$ $a\langle 100\rangle_H$ APB's of the Heusler phase.
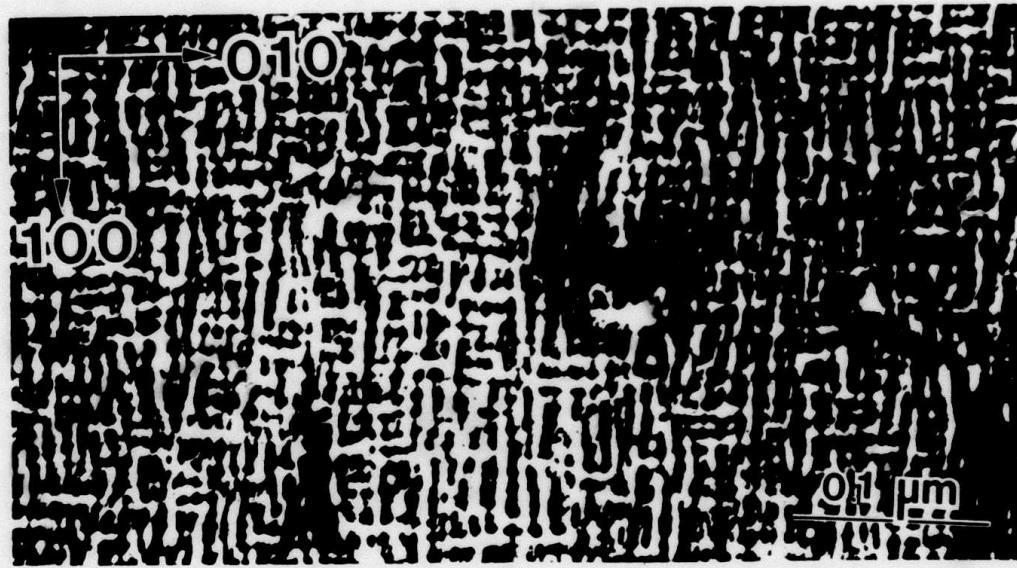


**Figure 2.** $200_H/100_{B2}$ dark-field micrograph of the alloy annealed for 10 min. at 800°C showing anisotropic modulation of the precipitated B2 phase (white contrast) and the Heusler phase along $\langle 100\rangle$ directions.
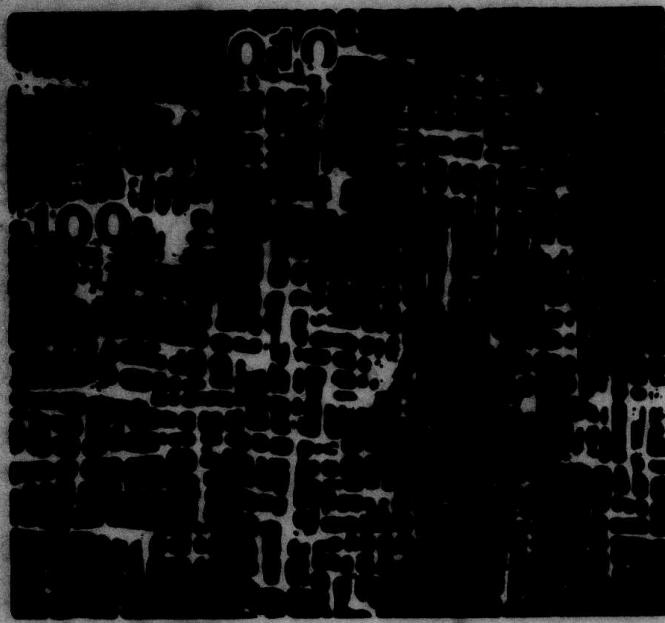
Figure 3. $200_H/100_{B2}$ dark-field micrograph of the 1 h annealed alloy showing interconnected B2 phase (matrix) and cuboidal particles of the Heusler phase.



Figure 4. Weak-beam dark-field micrograph ($004_H$ fundamental reflection) showing only bulk dislocations and no stress-accommodating dislocations. Same specimen as Figure 3.



Figure 5. $200_H/100_{B2}$ dark-field micrograph of the 10 h annealed alloy showing essentially the same micro-structure as for 1 h (Figure 3).
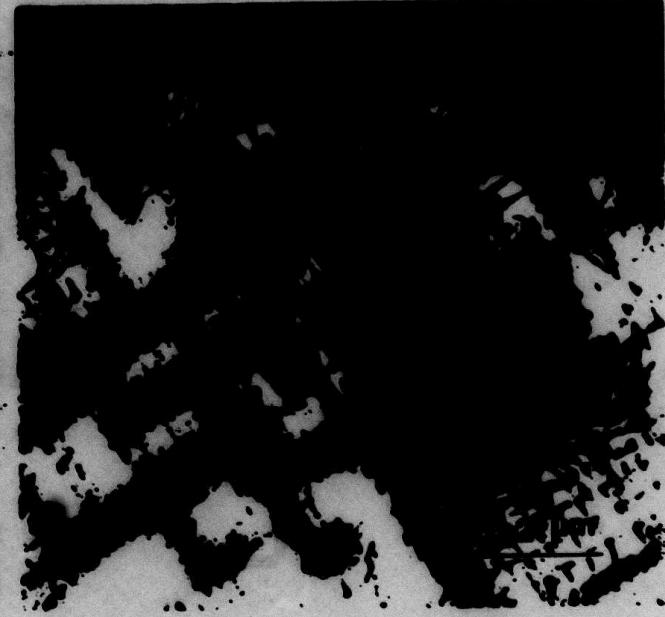


Figure 6. Bright-field image showing square net of interfacial dislocations in the alloy annealed for 10 h.
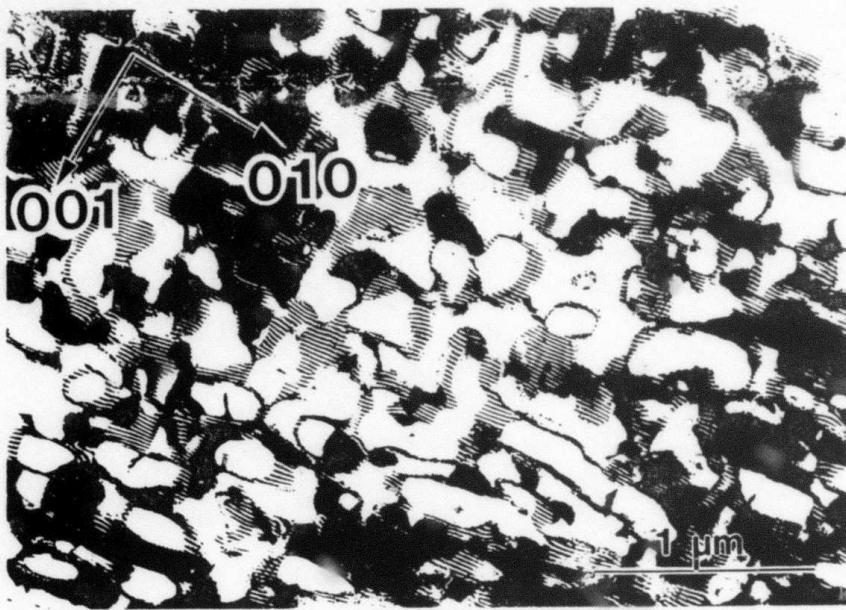
Figure 7. Dark-field micrograph (with $002_H/001_{B2}$ reflection) showing the almost isotropic two-phase interconnected structure, after 100 h annealing.
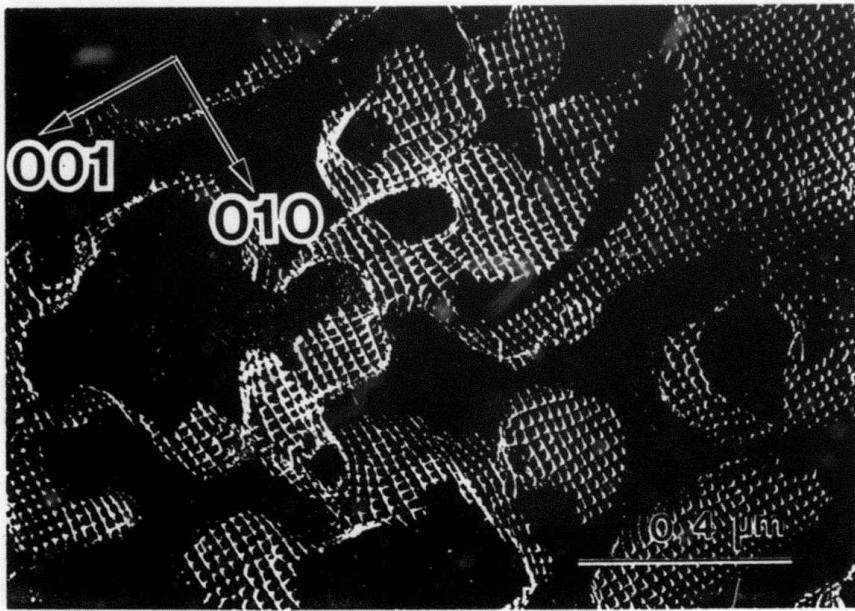


Figure 8. Weak-beam dark-field image of interfacial dislocations (b = a/2 <001>) with spacing small enough to reduce greatly misfit strain. Same sample as Figure 7.
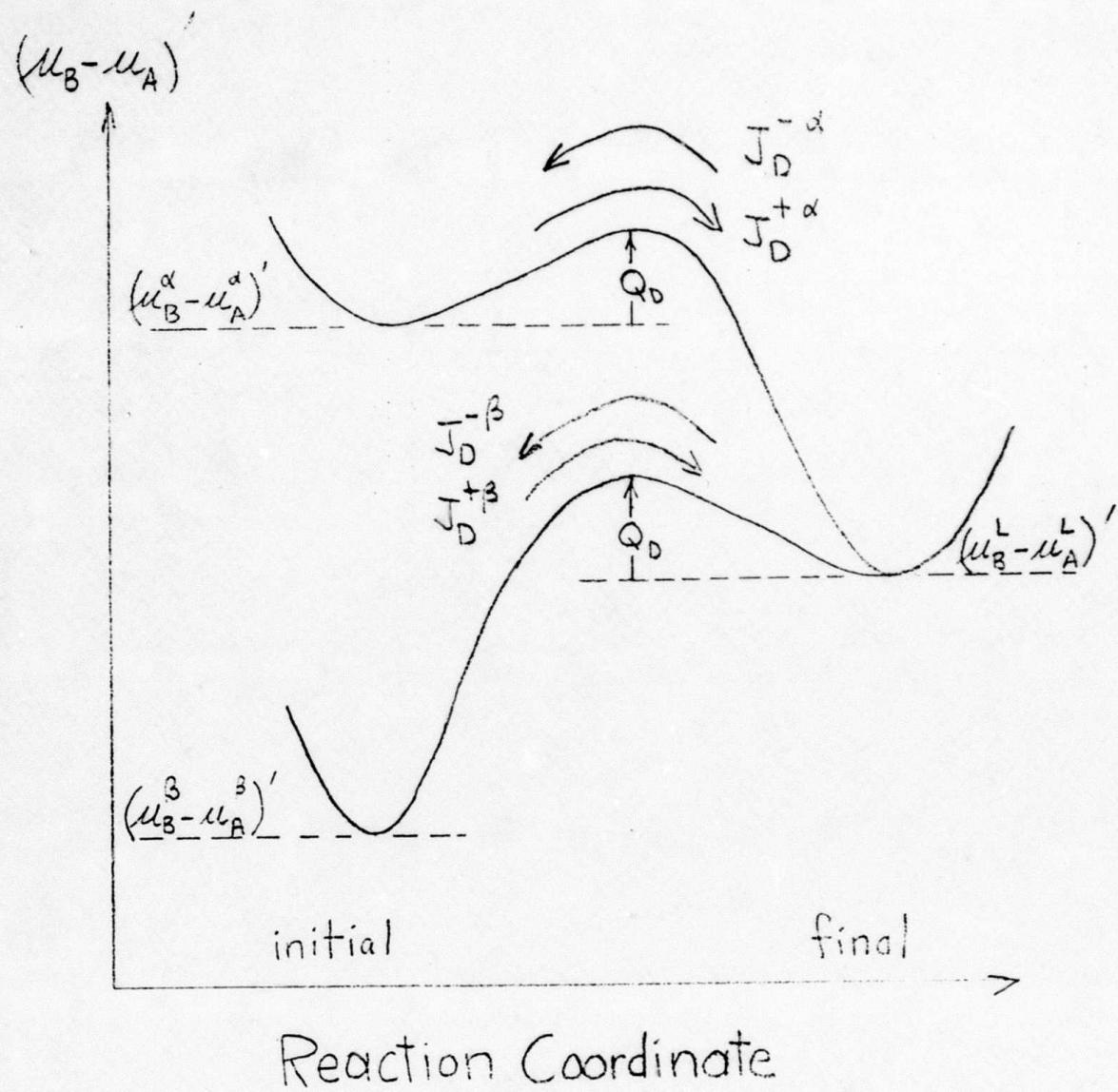
Figure 1. Reaction coordinate diagram for interface redistribution reaction. Initial states: B on $\alpha$ or $\beta$ site in solid, A in liquid. Final states: A on $\alpha$ or $\beta$ site in solid, B in liquid.
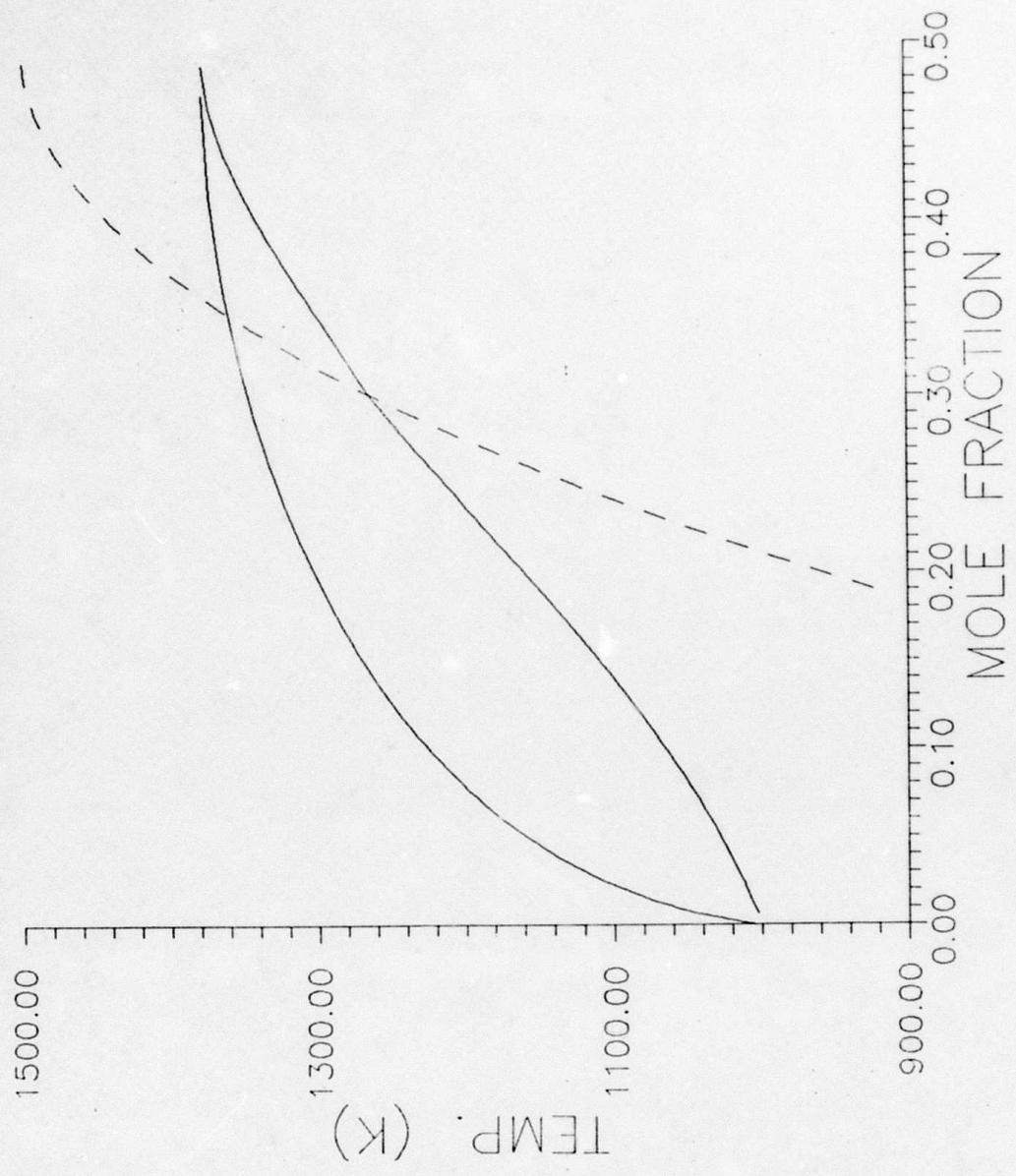
Figure 2. Calculated symmetric binary phase diagram for an ideal liquid in equilibrium with a Bragg–Williams phase with $T_c = 1500$ K. Pure component melting points are 1000 K and entropies of fusion are 2 R.
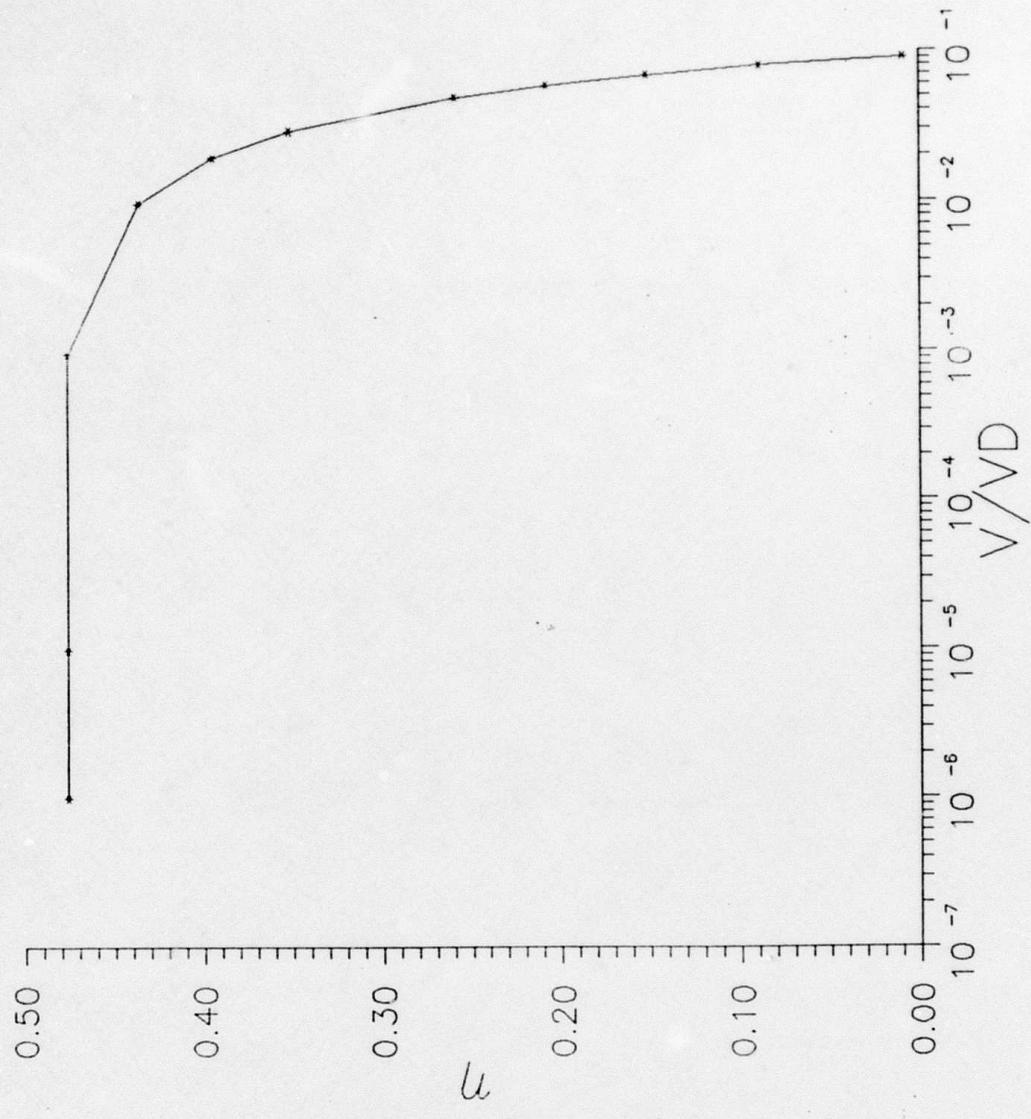
Figure 3. Long range order parameter of the solid at the interface, $\eta$, as a function of dimensionless growth velocity, $V/V_D$ for the congruently melting compound at $x_B^S = 0.5$ with equilibrium order parameter at the solidus; $\eta_e$, of 0.47. Calculated from Eqn. 35.
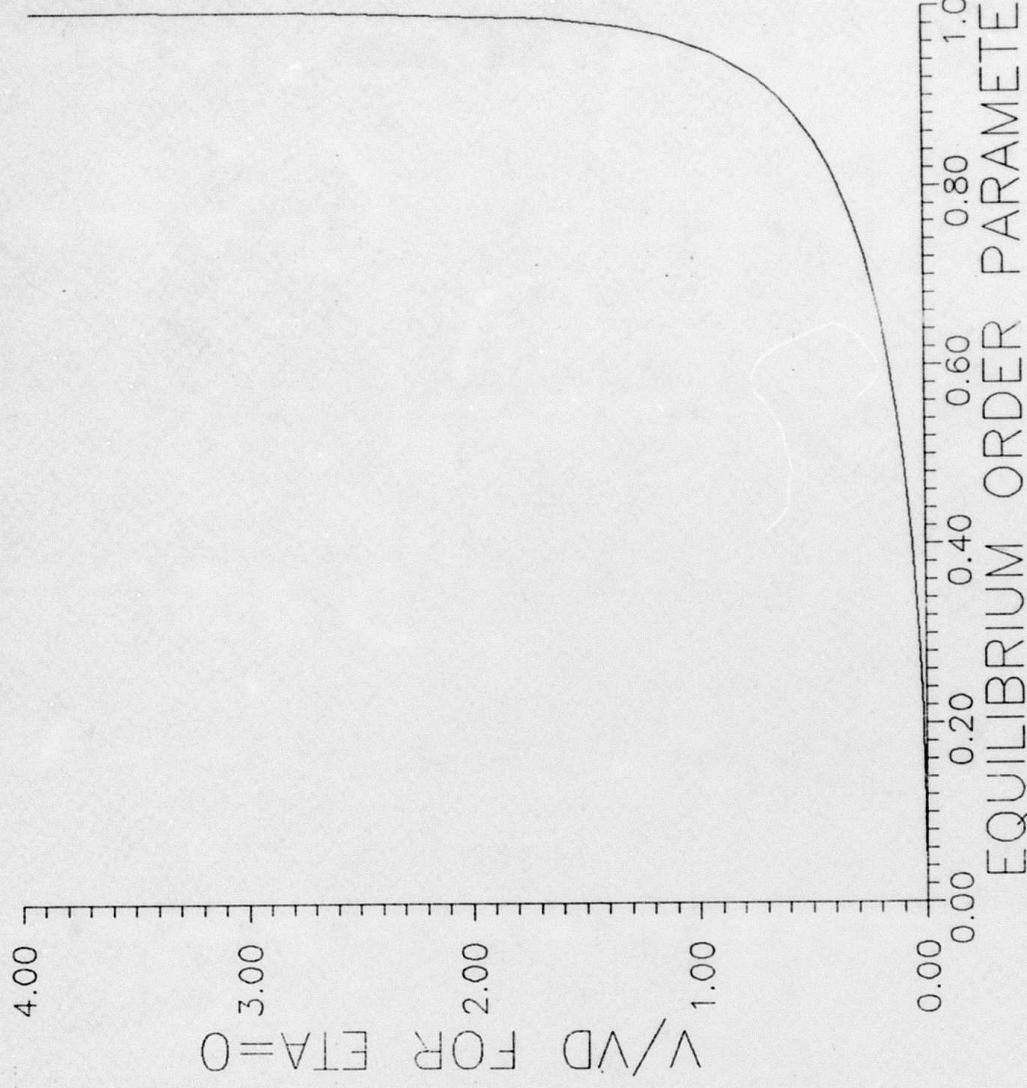
Figure 4. Dimensionless solidification velocity, $V/V_D$, required to completely suppress long range order in the solid at the liquid solid interface as a function of equilibrium order parameter.
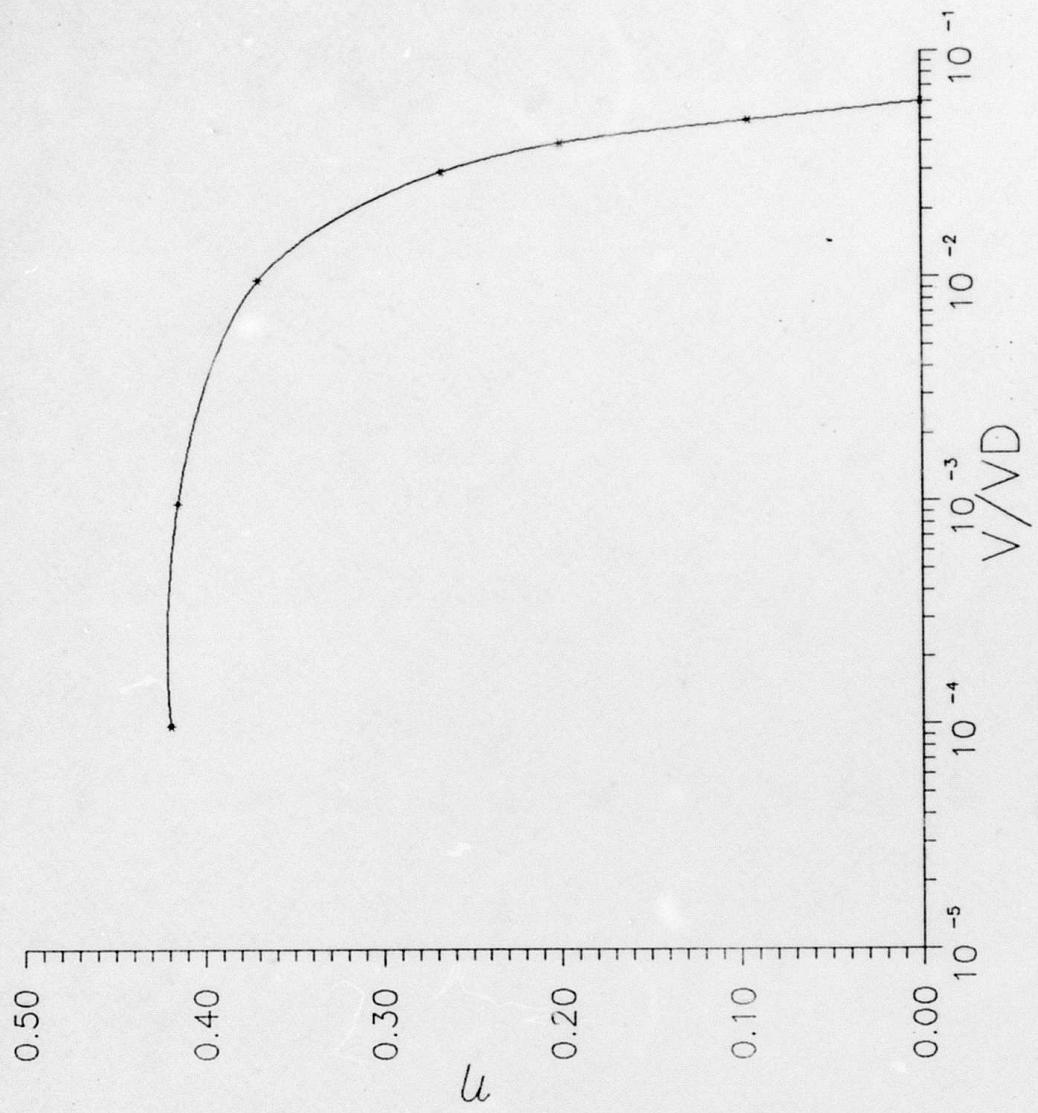
Figure 5. Long range order parameter of the solid at the interface, $\eta$, as a function of dimensionless growth velocity, $V/V_D$ for the system given in Figure 2 with $x_B^S = .415$, with $V_c = \infty$.
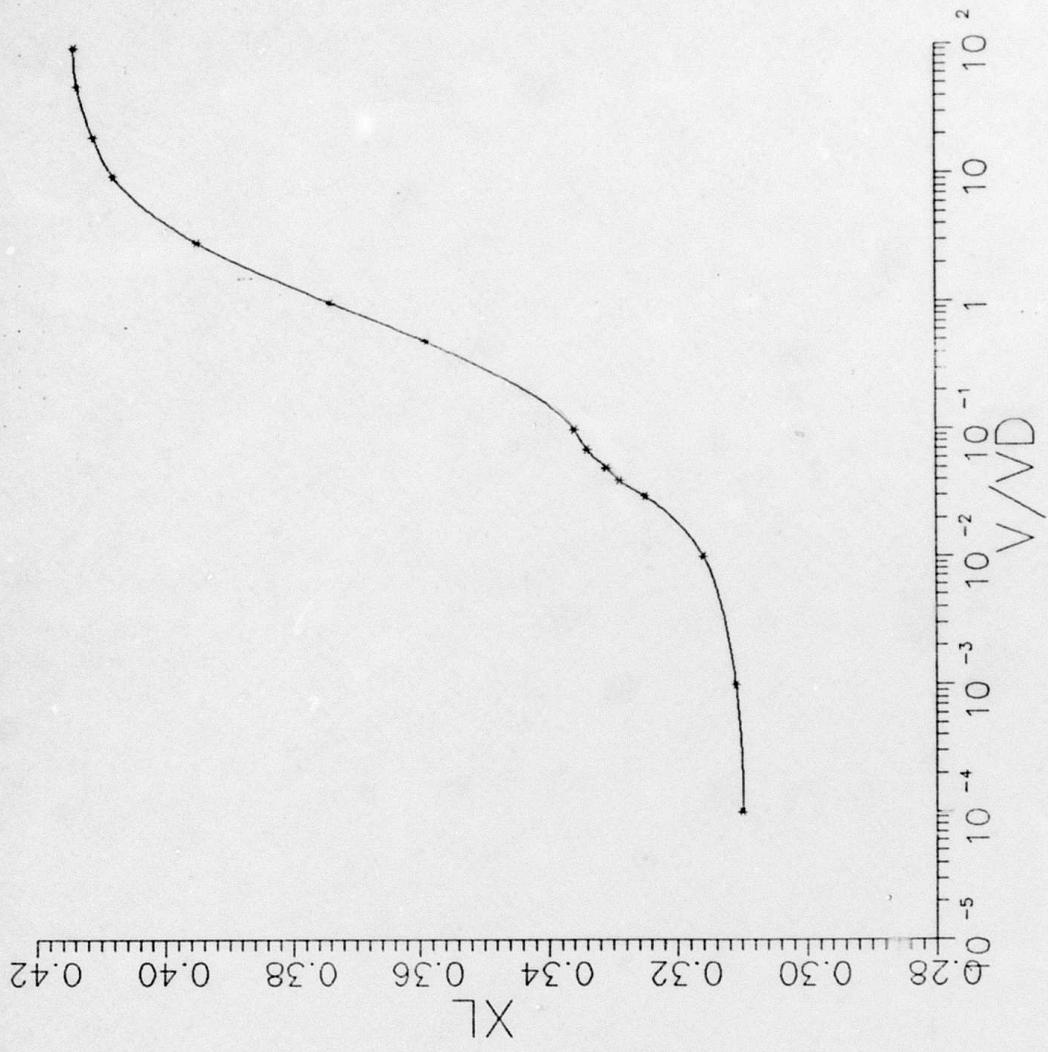
Figure 6. Liquid composition at the interface, $x_B^L$, as a function of dimensionless growth velocity, $V/V_D$, for the system given in Figure 2 with $x_B^S = .415$, and with $V_c = \infty$.
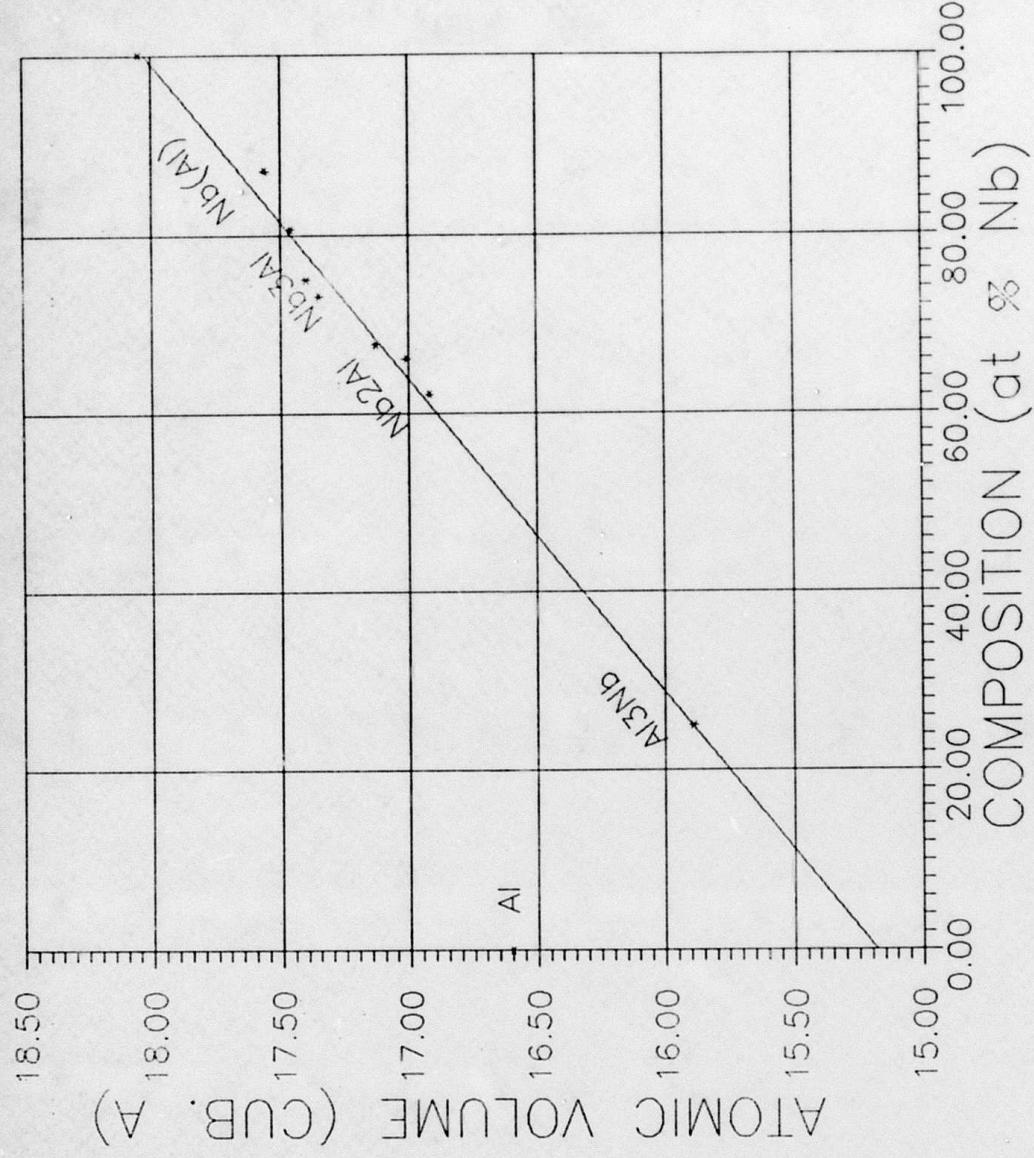
Figure 7. Atomic volume (unit cell volume/number of atoms per unit cell) versus composition for the phases in the Al–Nb system with a linear best fit excluding pure Al.
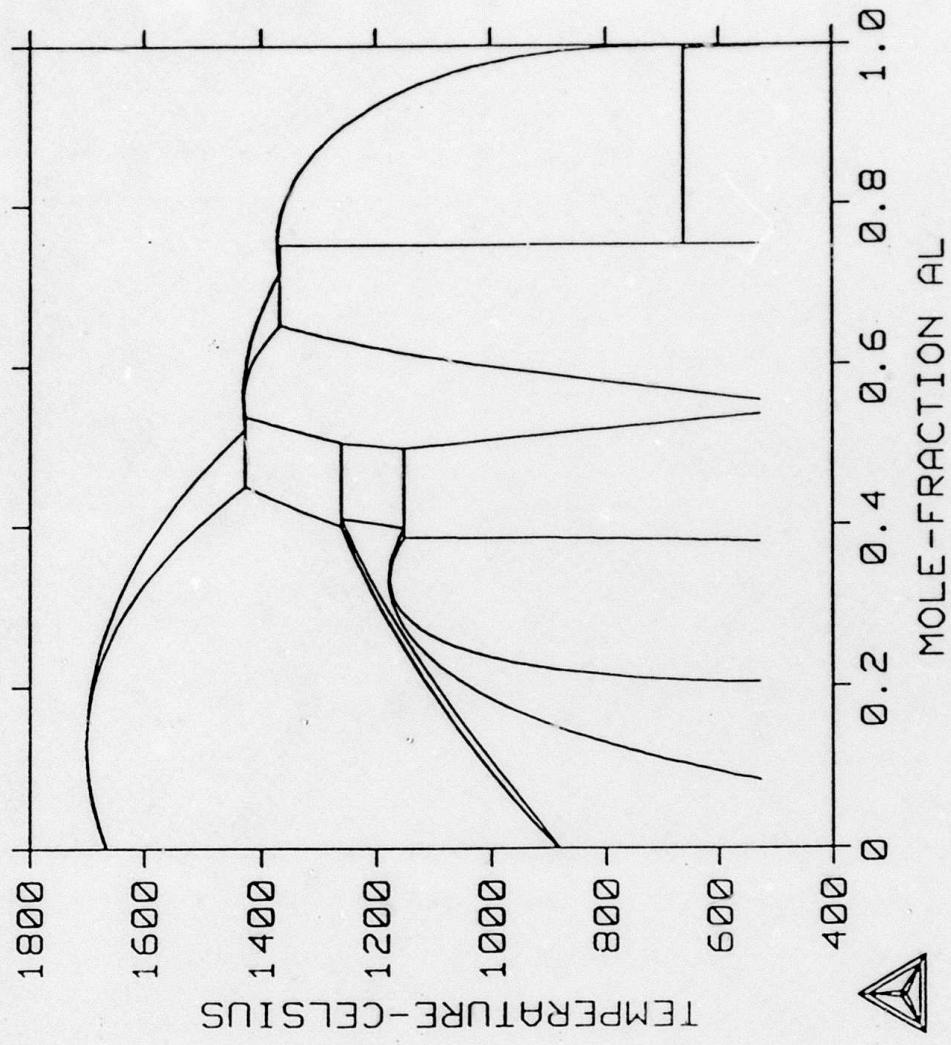
Figure 8. Calculated Ti–Al phase diagram used for calculation of Ti–Al–Nb ternary diagram.

THERMO-CALC (87.12. 7:15.42) :
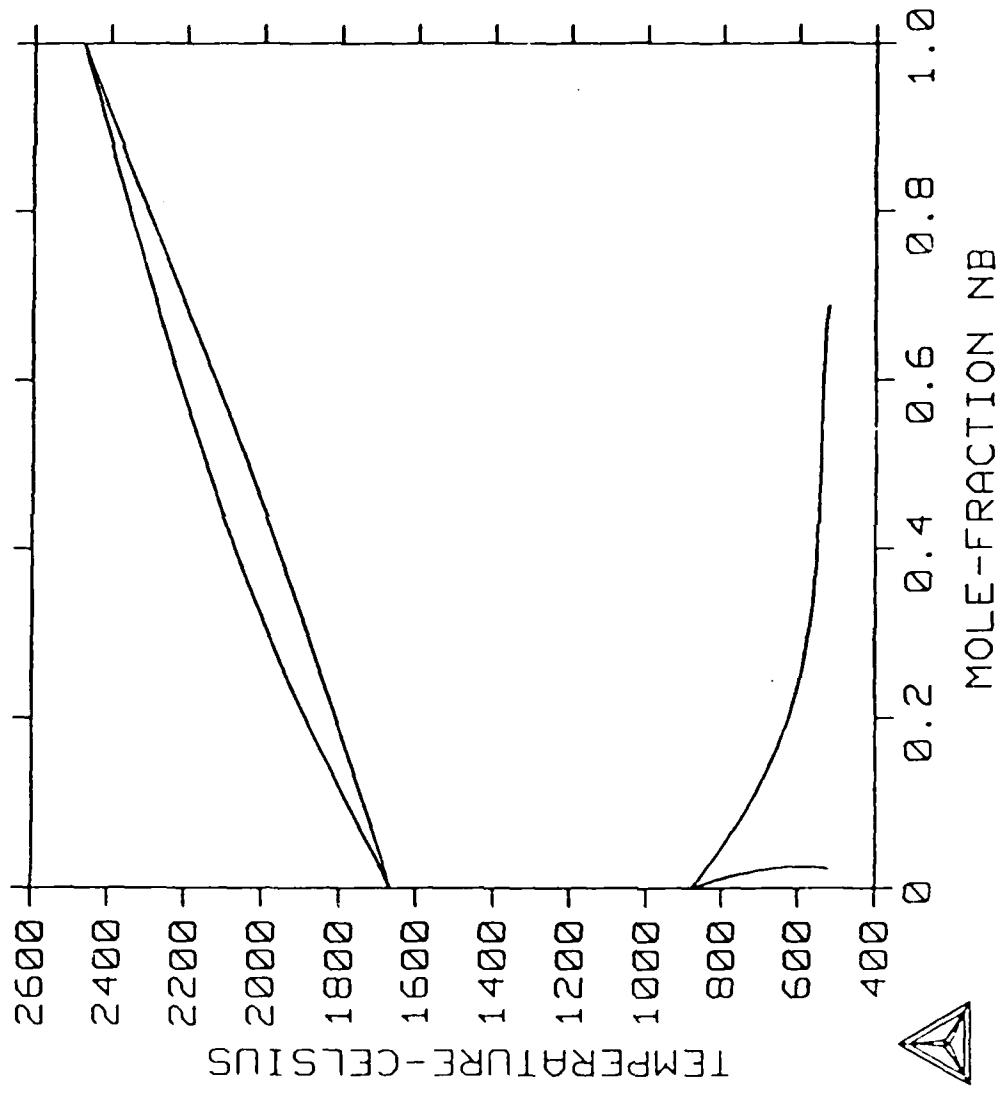


Figure 9.  Calculated Ti–Nb phase diagram used for calculation of Ti–Al–Nb ternary diagram.

THERMO-CALC (87.12.22:15.32) :
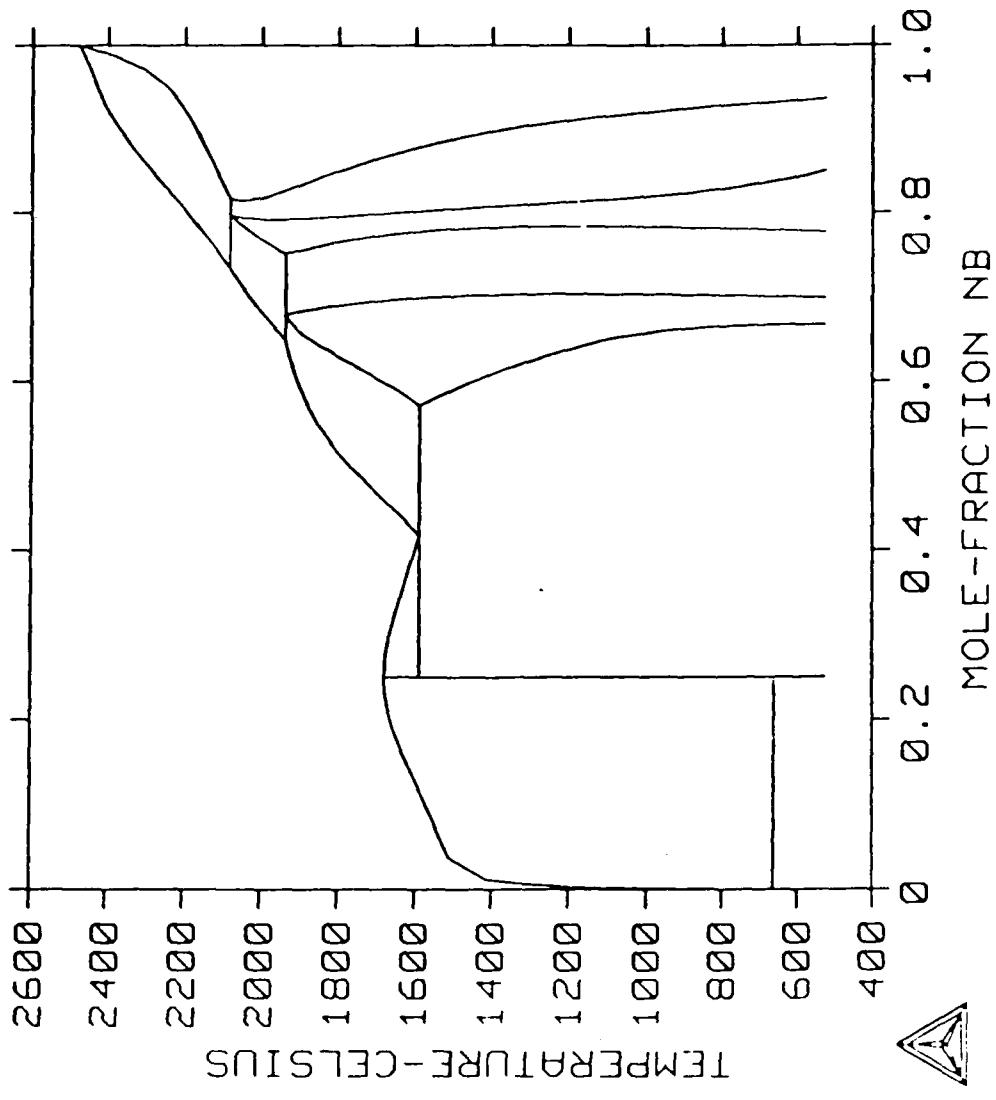
Figure 10. Calculated Nb–Al phase diagram used for calculation of Ti–Al–Nb ternary diagram.

THERMO-CALC (87.12.31:16.40) : 800°C
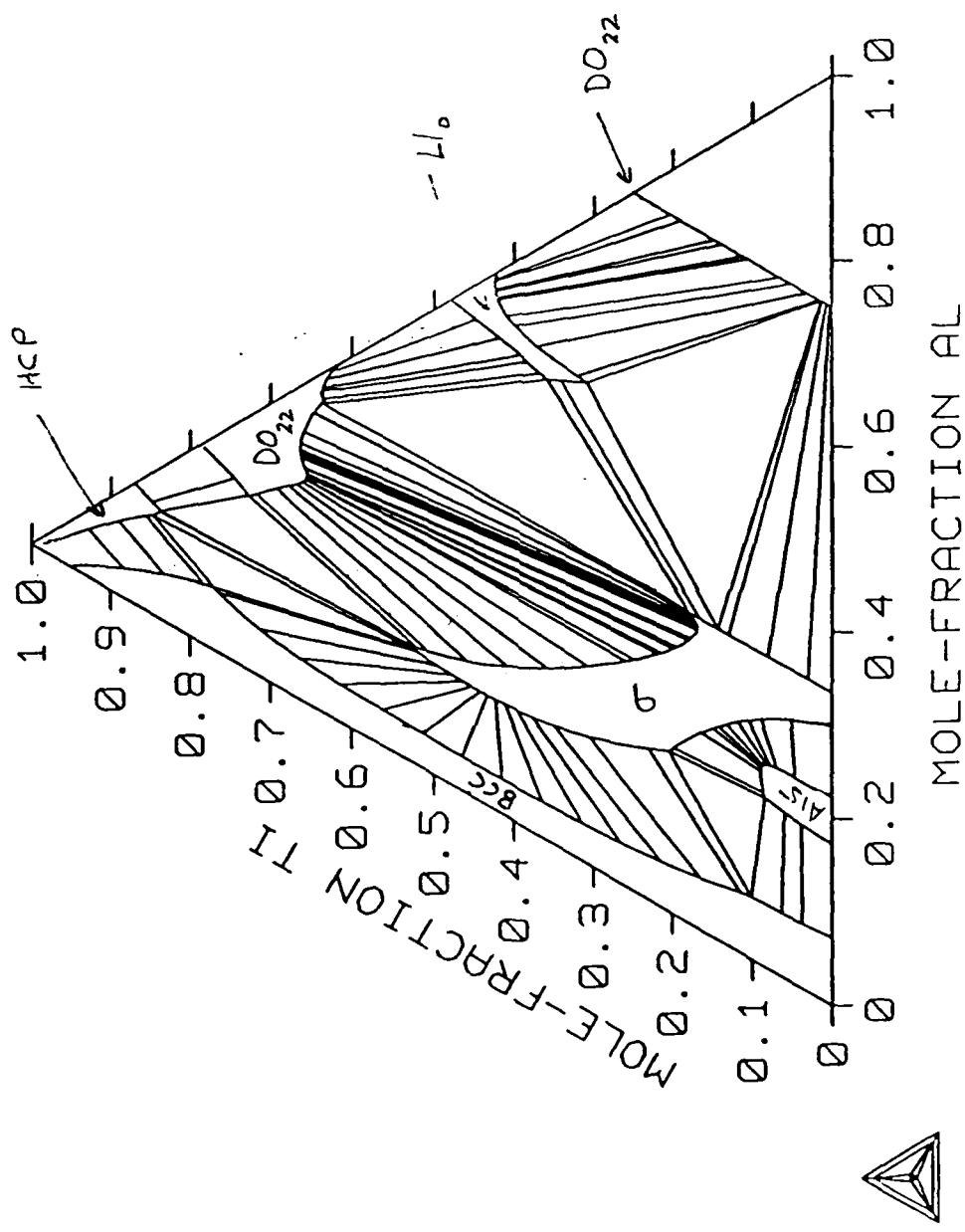
Figure 11. Calculated isothermal section of the Ti–Al–Nb ternary phase diagram at 800°C omitting ternary phases.

THERMO-CALC (8?.12.31:12.35) : C6 *1200 ℃*
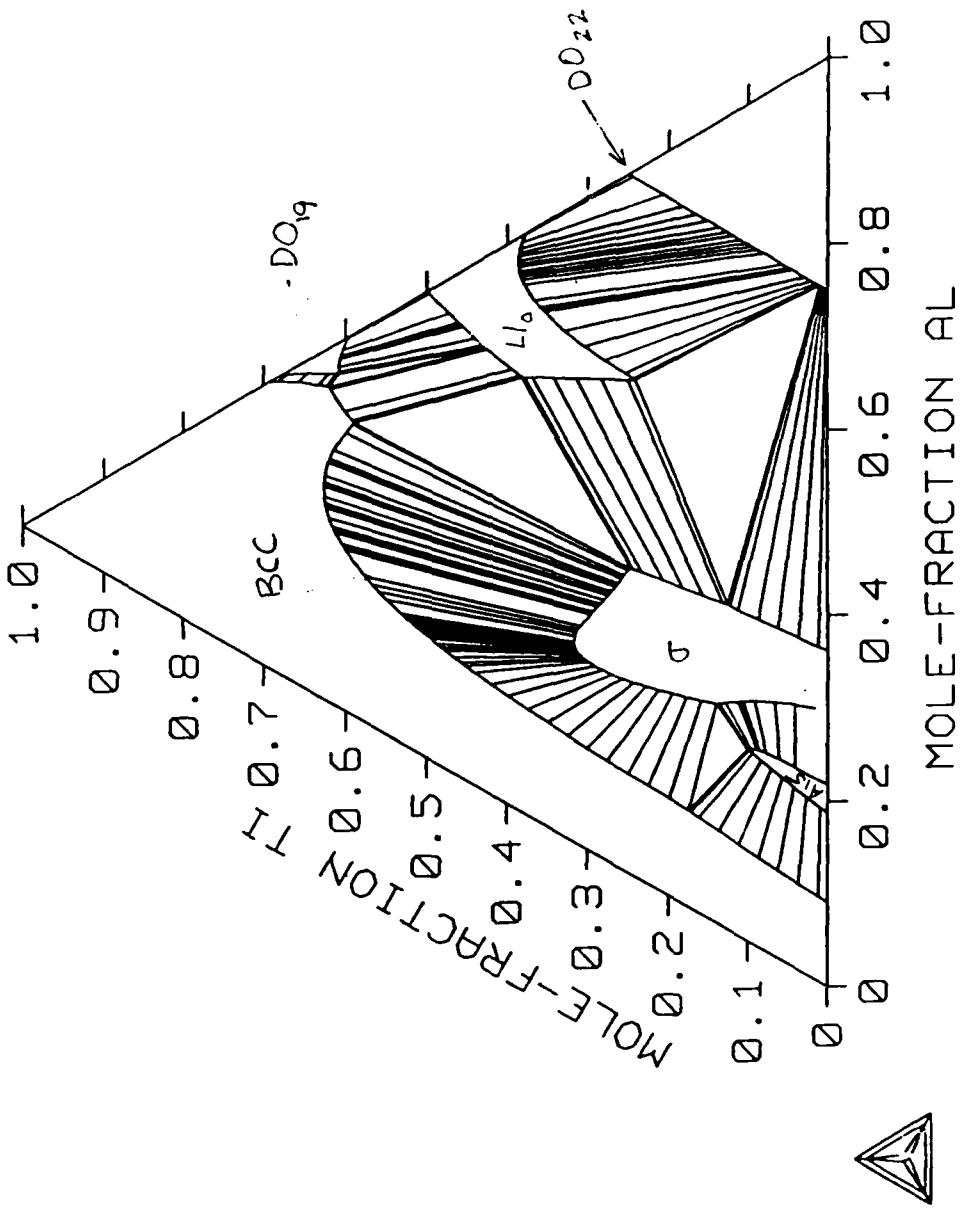


Figure 12. Calculated isothermal section of the Ti–Al–Nb ternary phase diagram at 1200° C omitting ternary phases.

THERMO-CALC (87.12.30:15.50) :
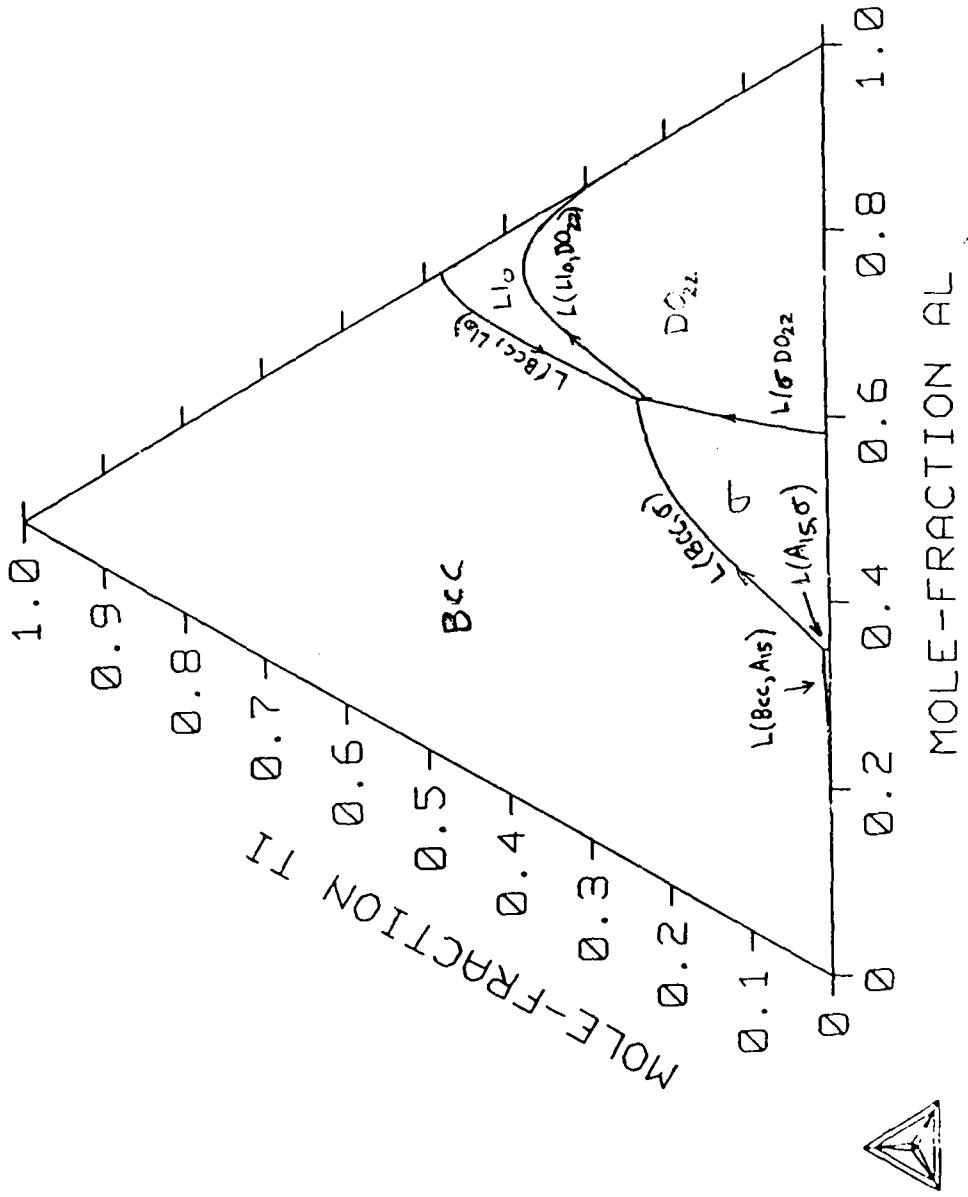


Figure 13. Calculated Equidus projection of the Ti–Al–Nb ternary phase diagram omitting ternary phases.

Reaction Scheme derived from liquidus projection and isothermal sections at 1200 and 800°C

| No-Al | Nb-Ti-Al | Ti-Al | Nb-Ti |
|---|---|---|---|

**No-Al column:**

L + bcc → A15

L + A15 → G

L → G + DO22

**Nb-Ti-Al column:**

L + A15 → bcc + G

A15 + bcc + G

L + bcc + G

L + bcc → G + L1o

L + L1o + G

bcc + G + L1o

L + G → L1o + DO22

G + L1o + DO22

bcc + G + L1o → hcp

bcc + G + hcp

G + L1o + hcp

L1o + hcp → G + DO19

L1o + G + DO19

G + hcp + DO19

**Ti-Al column:**

L → L1o + bcc

L → L1o + DO22

bcc + L1o → hcp

hcp → L1o + DO19

Figure 14. Reaction scheme for Ti–Al–Nb derived from the calculated liquidus projection and isothermal sections at 800°C and 1200°C.

Figure 15. The four atomic positions obtained by stacking eight small body–centered cubes. The sites a, b, c. d refer to the crystal structures in Table 3. The tetrahedron 123 is an example of the basic cluster used for the CVM calculation. It includes first–neighbor interaction 1–3 and 2–4 as well as second–neighbor interaction 1–2 and 3–4.